Protein structure, a genetic encoding for glycosylation

Benjamin P. Kellman,[1,2,3,4,5,*] Daniel Sandoval,[6] Olga O. Zaytseva,[7] Kelly Brock,[8] Sabyasachi Baboo,[9] Daniela Nachmanson,[2,3,10] Edward B. Irvine,[5,11] Erick Armingol,[1,2,3] Nathan Mih,[2,3] Yujie Zhang,[1] Mia Jeffris,[1,2] Philip Bartels,[6] Thi Nguyen,[6] Amy Tam,[8] Sarah Gasman,[12] Shlomi Ilan,[5] Isaac Shamie,[1,2,3] Jolene K. Diedrich,[9] Xiaoning Wang,[9] Esther van Woudenbergh,[5] Meghan Altman,[13] Anthony Aylward,[2,3] Bokan Bao,[1,2,3] Andrea Castro,[2,3] James Sorrentino,[1,2,3] Austin Chiang,[1,2] Matt Campbell,[14] Yannic Bartsch,[5] Patricia Aguilar-Calvo,[13,15,16] Christina Sigurdson,[13,15] Galit Alter,[5] Gordan Lauc,[7] John R. Yates III,[9] Debora Marks,[8,17] Frederique Lisacek,[18,19] Nathan E. Lewis[1,2,3,*]

[1] Department of Pediatrics, University of California, San Diego, La Jolla, CA 92093, USA
[2] Department of Bioengineering, University of California, San Diego, La Jolla, CA 92093, USA
[3] Bioinformatics and Systems Biology Graduate Program, University of California, San Diego, La Jolla, CA 92093, USA
[4] Augment Biologics, La Jolla, CA 92092
[5] Ragon Institute of MGH, MIT, and Harvard, Cambridge, MA, USA
[6] Department of Cellular and Molecular Medicine, University of California, San Diego, La Jolla, CA 92093, USA
[7] Genos Glycoscience Research Laboratory, Borongajska 83H, Zagreb 10000, Croatia
[8] Department of Systems Biology, Harvard Medical School, Boston, MA, USA
[9] Department of Molecular Medicine, The Scripps Research Institute, La Jolla, California 92037, United States
[10] Moores Cancer Center, University of California San Diego, 3855 Health Science Drive, San Diego, CA, 92093, USA
[11] Department of Immunology and Infectious Diseases, Harvard T.H. Chan School of Public Health, Boston, MA, USA
[12] Department of Pediatrics, Boston Medical Center, Boston, MA, USA
[13] Department of Chemistry and Biochemistry, University of California San Diego, 9500 Gilman Drive, La Jolla, CA, USA
[14] Institute for Glycomics, Griffith University, Queensland, Australia
[15] Department of Pathology, University of California San Diego, 9500 Gilman Drive, La Jolla, CA, USA
[16] Department of Neurobiology, The University of Alabama at Birmingham, Birmingham, AL 35243
[17] Broad Institute of Harvard and MIT, Cambridge, Massachusetts 02142, United States
[18] Proteome Informatics Group, Swiss Institute of Bioinformatics, CH-1227 Geneva, Switzerland
[19] Computer Science Department & Section of Biology, University of Geneva, route de Drize 7, CH-1227, Geneva, Switzerland

Summary (150 words)

Unlike DNA, RNA, and proteins, the dogma describes glycosylation as metabolically determined and unconstrained by template molecules. Without template-based expectations for glycan structures, research is hampered, obscuring how these critical molecules impact the behavior in thousands of human glycoproteins. Here, we challenge the assertion of template-free glycosylation and discover protein-encoded rules for glycan biosynthesis, by quantifying associations between glycan and protein features, which we call "glycoimpact." We estimate 45-55% of amino acids substitutions will minimally change protein structure, but significantly impact glycosylation. We find that "glycoimpact" influences canonical substitution matrices and genetic variant pathogenicity. We identify thousands of high-glycoimpact pathogenic variants spanning hundreds of diseases, including several linked to aberrant glycosylation including Oculocutaneous Albinism, Prion, and Gaucher's Disease. We also successfully predict glycosylation in HIV, SARS-CoV-2, and immunoglobulins. Overall, we present rules defining a genetic encoding for glycosylation, enabling glycan prediction and discovery of glycoprotein functions in health and disease.

Abstract

DNA, RNA, and proteins are synthesized using template molecules, but glycosylation is not believed to be constrained by a template. However, if cellular environment is the only determinant of glycosylation, all sites should receive the same glycans on average. This template-free assertion is inconsistent with observations of microheterogeneity—wherein each site receives distinct and reproducible glycan structures. Here, we test the assumption of template-free glycan biosynthesis. Through structural analysis of site-specific glycosylation data, we find protein-sequence and structural features that predict specific glycan features. To quantify these relationships, we present a new amino acid substitution matrix that describes "glycoimpact" -- how glycosylation varies with protein structure. High-glycoimpact amino acids co-evolve with glycosites, and glycoimpact is high when estimates of amino acid conservation and variant pathogenicity diverge. We report hundreds of disease variants near glycosites with high-glycoimpact, including several with known links to aberrant glycosylation (e.g., Oculocutaneous Albinism, Jakob-Creutzfeldt disease, Gerstmann-Straussler-Scheinker, and Gaucher's Disease). Finally, we validate glycoimpact quantification by studying oligomannose-complex glycan ratios on HIV ENV, differential sialylation on IgG3 Fc, differential glycosylation on SARS-CoV-2 Spike, and fucose-modulated function of a tuberculosis monoclonal antibody. In all, we show glycan biosynthesis is accurately guided by specific, genetically-encoded rules, and this presents a plausible refutation to the assumption of template-free glycosylation.

Introduction

DNA, RNA, and protein synthesis follow DNA and RNA templates. However, glycosylation is considered non-templated, assumed to be primarily regulated by the cellular environment.[3] This assertion leads to a dilemma. If glycan biosynthesis is template-free, all glycosylation sites on a protein should have similar glycans with some stochastic variation. Yet, each specific site on a protein can reproducibly host different glycans, a phenomenon termed "glycosite-specific microheterogeneity."[4]

Though the template-free hypothesis remains, many observations show protein structure influences glycosylation. For example, protein primary sequence influences glycan diversity and identity. In the N-glycosylation sequon,[5] glycans covalently attach to asparagines (N) with a downstream (N+2) serine (S) or threonine (T) separated by any amino acid (X) except proline (NX[S/T]). Variation at N+1 impacts glycan complexity[6] and accessibility impacts glycosite occupancy.[7] Glycosylation of sequons ending in threonine is ~40 times more efficient than those with serine.[8] Upstream of the glycosite, a phenylalanine to alanine substitution in human IgG3 can increase bi-galactose structures with a core-fucose.[9] Additionally, influenza evolves hemagglutinin glycosylation sites to facilitate immune evasion.[10] Glycoprotein-determined glycan evolution, used by HIV for immune evasion, has been leveraged to engineer better vaccine epitopes.[11] Tools like GlycoSiteAlign[12] and mutagenesis studies have offered expansions of the founding sequon structure (NX[S/T]) including the enhanced aromatic sequon—an aromatic residue upstream of the glycosite (N-2) that can influence glycan complexity[13] with a variable impact given the N+1 variation.[14] In prediction, several works since 2002 have shown variable success in predicting glycosites from sequons and hidden features using machine learning,[15–18] though none have predicted beyond glycosite presence or the root monosaccharide.

Beyond the primary sequence, secondary structures (β-sheets and α-helixes) can influence glycosylation[19] while concavity, accessibility and hydrophobicity also impact glycosite occupancy.[7] ERManI (MAN1B1) and Golgi Mannosidase IA (MAN1A1), crucial bottlenecks in glycan processing, have been co-crystalized with a Man9 glycan to study specific glycoconjugate features that permit or inhibit this interaction.[20–23] A study of >150 glycoproteins revealed differential glycosylation as a function of protein structure, wherein low accessibility sites impacted core fucosylation and branching;[24] similar accessibility constraints predicted oligomannose on the SARS-CoV-2 spike protein.[25] Also, a structural analysis found FUT8 activity is impacted by glycosite depth.[26] Site-specific kinetics for glycosylation of Protein Disulfide Isomerase[27–29] and five additional glycoproteins[30] further showed that protein structure influences occupancy. Recent studies have shown interest is grafting glycans to proteins.[17,31–33] These

77 approaches provide valuable instruments for exploring mechanistic and steric associations between
78 glycans and folded proteins. Yet, they do not explore generalizable associations between glycan and
79 protein structure features that can be mapped back to the genome.

80 These studies represent a growing refutation of non-templated glycan biosynthesis. However, they have
81 not been consolidated into an interoperable mapping from the genome to the glycome. Here, we define
82 rules governing glycosylation by analyzing trends in site-specific glycosylation[34] in the context of glycan
83 biosynthesis[35] and site-specific protein structure features.[36] We describe this genetic encoding for
84 glycosylation as a mapping from "glycoimpactful" protein structure to expected glycan structures. We
85 validate these glycoimpact relations by comparison to evolutionary substitution matrices, variant
86 pathogenicity scores, and glycosite co-evolution. Further, we find that glycosite-proximal pathogenic
87 variants correspond to higher glycoimpact substitutions. Finally, we use glycoimpact to accurately
88 predict changes in glycan complexity, galactosylation, sialylation and functional glycosylation. Taken
89 together, we present a comprehensive argument for updating our understanding of glycosylation from
90 template-free, to bounded biosynthesis. Under bounded glycan biosynthesis, a range of feasible glycans
91 are "requested" by local protein structure and are "fulfilled" contingent on precursor availability (**Figure**
92 1); biosynthetic constraints represent a genetic encoding, making glycans predictable for any biologist.

93

94 Results

95 Constructing a database containing paired protein and glycan structures

96

97 We first tested if glycan structure correlates with protein structure. To do this, we built the Protein-
98 Glycan Enriched Structure Database (PGES-DB), a compendium of experimentally measured and expert
99 curated site-specific glycoprofiles on human glycoproteins collected from UniCarbKB[38] and GlyConnect[34]
100 databases (**see Methods**). Glycan structures were decomposed into substructures (i.e., biosynthetic
101 intermediates) using GlyCompare. This maximizes statistical power by making explicit every permissible
102 precursor molecule at each site.[35] Glycosite-proximal protein structure features were extracted from
103 protein structure models, and proximity was defined by minimum distance—the minimum 3D Euclidean
104 distance between the nearest atoms in each residue. The resulting PDES database includes 98
105 glycoproteins with N-glycosylation sites and 38 glycoproteins with O-glycosylation sites and a total of

106 3,563 N-glycosylation and 700 O-glycosylation events (Supplementary **Figure** 1). In this work, we limited
107 training to human glycoproteins and limited predictions to glycoproteins expressed in humans.

108 We verified that the glycan-annotated glycosites in PGES-DB are representative of all glycosite
109 structures in the human secretome;[39] all secretome glycosites fall within a dimensionality reduction
110 trained only on PGES-DB glycosite structures (**Figure** 2a, see **Supplementary Results**, Supplementary
111 **Figure** 2). Thus, PGES-DB can provide generalizable conclusions about protein-glycan associations.
112 Furthermore, we examined the associations (termed "intermolecular relations (**IMR**)") between glycan
113 substructures (e.g., tri-mannose) and glycosite-proximal protein features (e.g., proximal tyrosine) within
114 PGES-DB, and we found that glycan substructures and protein features were significant and substantial
115 (Supplementary **Figure** 3a). Fisher exact test found 10,111 substantial and significant IMR with 9,296
116 positive and 815 negative associations (**Figure** 2b). Using multiple statistical tools (including Fisher's
117 Exact Test, conditional probability, and information gain, see **Supplementary Results**), we confirmed
118 that PGES-DB contains many notable IMR.

119 Highly deterministic IMR are consistent with canonical templating

120 We found several highly deterministic amino acid (AA) specific intermolecular relations (IMR) ((Pr(G|P)
121 is 0.999-1 or 0-0.001). In these high-confidence IMR (hcIMR), the impact of precursor-limitation is
122 minimal, so the protein-imposed "requests" are more easily "fulfilled" and observed. Overall, confidence
123 in glycan presence increases when a specific protein structure feature is present (Supplementary **Figure**
124 4). For IMR with a spatially proximal AA (within 6A), 20.2% are highly deterministic of glycan
125 substructures. Additionally, 32.4% and 17.5% of down- and upstream AA IMR (+/-5aa) are highly
126 deterministic. The certainty with which an AA determines a glycan structure decreases substantially
127 when proximal AA are absent (Supplementary **Figure** 4**a**). These hcIMR are not dominated by small
128 numbers of motifs as the high-confidence IMR count is proportional to the number of unique
129 substructures (Supplementary **Figure** 4**b**). The decrease in hcIMR when a protein structure feature is
130 absent suggests bounded glycan biosynthesis is an active rather than passive process.

131 Among the highly deterministic protein-glycan relations, we observe (among 1,725 N-glycosylation
132 events) 1,553 glycans that contain a N-acetylglucosamine (GlcNAc) on the α-1,6-mannose branch
133 (Glc2NAc(β1-6)Man(α1-6)Man(β1-4)Glc2NAc); indicative of complex N-glycosylation. All 75 hcIMR with a
134 downstream tryptophan include glycans with the hybrid/complex substructure. These observations
135 suggest that tryptophan is sufficient to escape oligomannose structures. Similarly, in 454 O-glycosylation
136 hcIMR, 237 contain 6-sialyl-N-acetyllactosamine (Neu5Ac(α2-6)Gal(β1-3)GalNAc). Of 6 events

137 containing a sequence-proximal tryptophan, every event also contained a sialyl-T antigen. Thus, several
138 IMR link protein features, such as proximal tryptophan, with specific glycan features.

139 Glycosite-proximal structure and chemistry correlate with glycan structure

140 The numerous glycan-protein relations suggest the plausibility of bounded glycan biosynthesis. To
141 generate testable protein structural constraints on bounded glycan biosynthesis, we modeled IMR using
142 hierarchical regression to minimize relevant bias. We quantified specific IMR using univariate logistic
143 generalized estimation equations (GEE) to probe the site-matched glycan-protein co-occurrences in
144 PGES-DB and to control for protein identity effects (see **Methods**). A list of GEE odds ratios (OR) (each
145 describing the association between a protein structure and one of several glycan substructures)
146 describes the typical glycosylation near a given protein structure; the OR list indicates the "expected
147 substructure abundance" or an "expected glycoprofile" related to a glycosite-proximal protein structure.
148 When expected glycoprofiles are compared between two protein structures (e.g., the expected
149 glycoprofile difference between valine and isoleucine), we can estimate a glycosylation impact, or
150 "glycoimpact," of making amino acid substitutions or other protein feature changes. Glycoimpact is the
151 difference (z-score normalized Euclidean distance) in expected glycoprofiles between two protein
152 structures (**Figure** 3, see **Methods**).

153 We discovered 1,715 significant N-glycan IMR (FDR<0.1, |log(OR)|>0.1), many of which were associated
154 with spatially proximal (N+6Å) and sequence-proximal AA (N+/-5 residues). Stratifying sequence-
155 proximal effects, we observed almost twice as many IMR involving upstream (N-5) than downstream
156 (N+5) AA. Among the downstream AA effects, tryptophan, alanine, serine, and phenylalanine are most
157 impactful (99, 55, 55, and 48 IMR respectively). Tryptophan also has many IMR when downstream or
158 spatially proximal (26). Spatially proximal arginine (70) and downstream glutamine (35) are the largest
159 effectors. Finally, glycosylation sites on turns have many IMR (61) (**Figure** 2c).

160 Turn-associated IMR include >3-fold increases in di- and tri-sialylated tetra-antennary and >2-fold
161 increases in mono- and di-galactosylated structures with core fucose; all positively correlated structures
162 have at least one galactose while not all are core fucosylated. Structurally proximal glutamine is
163 associated with a >20-fold increase in monosialylated triantennary structures and a 10-fold decrease in
164 tetraantennary structures (**Figure** 3**a**). Histidine, threonine, and valine show correlation with increasing
165 GalNAc[4S] (**Figure** 3**b**). Expanding on **Figure** 3a-b, we further interrogated IMR for specific protein
166 structure features (i.e., proximal amino acid or local secondary structure) by comparing the IMR odds
167 ratio to monosaccharide count for several monosaccharides (**Figure** 3**c**). A biclustering highlights two

168 major types of protein structure influence, mirroring the N-glycan/O-glycan dichotomy in glycosylation.
169 Providing clues to the elusive O-glycosylation site, proximal alanine is negatively correlated with
170 galactose and GlcNAc but positively correlated with N-acetylgalactosamine (GalNAc). Conversely,
171 threonine and histidine are positively associated with GlcNAc and galactose but negatively correlated
172 with β-GalNAc. As expected, GlcNAc and complex-glycans follow similar trends to Neu5Ac. However,
173 Neu5Ac, GlcNAc and Gal trends diverge near proline, cysteine, and valine; these amino acids may act as
174 limiters of high-complexity (**Figure** 3**c**).

175 Amino acid changes can predict glycan structural changes

176 We found that many AA-substitutions can have substantial "glycoimpact" (expected difference in
177 glycosylation) on glycan biosynthesis; exemplified by the phenylalanine-tryptophan substitution (**Figure**
178 3**d-e, Supplementary Results**). Upstream phenylalanine is associated with bi- and tri-antennary (>3-fold)
179 while upstream tryptophan is associated with tetraantennary terminal galactose (>2-fold) implicating
180 this substitution in branching (**Figure** 3**d**). Additionally, spatially proximal phenylalanine is strongly
181 associated with increased sialylation (>10-fold) implicating this amino acid in glycan maturation (**Figure**
182 3**e**). These predictions suggest that tryptophan-phenylalanine substitution has a large impact on
183 glycoprofiles.

184 We calculated all AA-substitution glycoimpact scores as the difference in expected glycoprofiles
185 between each AA-pair (see **Methods**, Supplementary **Figure** 5). Glycoimpact was calculated at multiple
186 IMR thresholds (Supplementary **Figure** 5). We highlight relevant substitution events as "glycoimpactful"
187 (significantly high glycoimpact) and structurally ambivalent (BLOSUM>0) (**Figure** 3**f**). As explained in the
188 next section, we call the glycoimpact AA-substitution matrix the BLOSUM-PAM Orthology matrix
189 (BLAMO X:Y); X and Y refer to the log odds ratio and FDR thresholds respectively. Sub-threshold odds
190 ratios, those insignificant or unsubstantial by the X:Y threshold, are excluded from the glycoimpact
191 calculation. **Figure** 3f displays a subset of BLAMO 0.5:0.1 relations.

192 Glycoimpact explains discrepancies between BLOSUM and PAM substitution matrixes

193 To further explore the relevance of glycoimpact, we compared it to conservation-based measures of
194 amino acid substitution impact. The PAM[41] and BLOSUM[42] AA substitution matrices are popular but
195 distinct estimates. PAM is based on global alignments within a protein and reflects more functional
196 conservation, while BLOSUM uses local alignment across proteins and highlights more structural
197 conservation.[43,44] Thus, these measures differ more when protein function is not fully described by
198 protein structure.

199 Since changes in glycan structure can modify protein function in a protein structure-independent
200 manner, we examined consistency between PAM and BLOSUM estimates across null and high
201 glycoimpact substitutions. Comparing PAM and BLOSUM scores at multiple thresholds
202 (RMSE($PAM_{i,j}$,$BLOSUM_{i,j}$)), we found that error in 4 of 5 PAM-BLOSUM comparisons was significantly
203 correlated to glycoimpact (BLAMO 0.5:0.1) for high-glycoimpact (GI>2.5) substitutions (**Figure 4a,**
204 Supplementary **Figure** 5). The correlation between high-glycoimpact substitutions and PAM-BLOSUM
205 inconsistency is maintained for most PAM and BLOSUM thresholds (Supplementary **Figure** 6). Both
206 protein structure and glycosylation are necessary to fully explain protein function, and these results
207 suggest a positive relationship between glycoimpact and the failure of structure (BLOSUM) to
208 completely explain function (PAM). Given this relationship, we refer to the glycoimpact substitution
209 matrix as the BLOSUM-PAM Orthology (BLAMO) matrix.

210 High glycoimpact residues are conserved around glycosites

211 If glycosite-proximal amino acids influence functional glycosylation, there should be evolutionary
212 pressure imposed beyond the classical NX[S/T] N-glycan sequon. To map the broader glycosite structure,
213 we aligned glycosites (**Figure 4b-c**) and examine conservation and evolutionary coupling (EC). Using EC
214 derived from 2,005 glycoprotein alignments (see **Methods**, **Supplementary Results**),[45] we observed
215 enriched coupling between N-glycosites and flanking residues (Supplementary **Figure** 7a). We also
216 observed several position-specific glycosite-coupled residues including serine and threonine at N+2,
217 phenylalanine at N-2, and tyrosine at N-1 (pooled hypergeometric, FDR<0.1, Supplementary **Figure** 7c,
218 **Figure 4c**). These findings are consistent with previous observations of the original sequon and
219 enhanced aromatic sequon.[14] Glycosite-coupled residues are also consistent with IMR-observed high-
220 impact residues (**Figure** 2**c**). Of the ten high-impact upstream residues, seven show enriched glycosite-
221 coupling when they appear upstream. To further highlight global glycosite structure, we clustered
222 glycosites using coupling probabilities (**Figure 4d,** Supplementary **Figure** 8, see **Methods**). The N+2
223 aspartic acid enriched in the univariate analysis (**Figure 4c**) co-occurs with an N-2 lysine (**Figure 4d,** motif
224 1). Alternatively, glutamic acid is more likely to co-occur with other glutamic acid residues (N -4, +1, and
225 +3) with an N+2 threonine sequon (**Figure 4d,** motif 4). These couplings are reflective of evolutionary
226 pressures surrounding the glycosylation sites.

227 We next aligned[12] glycosites permitting a tetraantennary N-glycan lacking fucose or sialic acids (**Figure**
228 **4b**). We examined the glycosite alignment for consistency with high-influence AA (**Figure 2c**) and
229 glycosite-coupled residues (**Figure 4c**). Of 20 glycosite-flanking AA, 16 show consistency between the

230 first or second most common AA and either the high-influence or glycosite coupled residues (see
231 **Supplementary Results**). At nearly every glycosite-flanking residue (N+/-10) there is consistency
232 between these three analyses, further corroborating that protein structure constrains glycosylation.

233 ## Glycoimpact correlates with discrepancy between functional variant predictions

234 Dozens of algorithms predict functional and pathogenic effects of genetic variants,[40,46,47] incorporating
235 information ranging from sequences to protein structure, thus sometimes reporting different variants as
236 deleterious. We hypothesized the differences in some pathogenicity scores between algorithms could
237 be explained by glycoimpact (BLAMO 0.5:0.1, see **Methods**). Across 3,549,910 nonsynonymous
238 mutations, we measured the disagreement (RMSE) between each of 27 rank-normalized functional
239 impact prediction tools, precomputed with dbNSFP;[40] pathogenicity score divergence was then
240 correlated with glycoimpact. After hierarchical clustering on the divergence-glycoimpact correlation
241 coefficients, pathogenicity estimates separated into two major clusters: one containing nearly all (6/7)
242 tools leveraging protein-structure and the other primarily containing conservation, sequence, and/or
243 epigenetic-based tools (**Figure** 5**b**). Nearly all variant pathogenicity score differences across the two
244 clusters correlated with glycoimpact. These correlations and clustering structure disappear when
245 glycoimpact scores are shuffled (Supplementary **Figure** 10); thus, like BLOSUM-PAM discrepancies,
246 glycoimpact correlates with discrepancies between conservation-based and protein structure-based
247 pathogenicity estimates. These observations further implicate glycosylation as a potent functional
248 regulator and glycoimpact as an appropriate proxy for the importance of glycosylation.

249

250 ## Glycoimpact proposes mechanisms for pathogenic variants in ClinVar and PrP

251 Because glycoimpact correlates with evolutionary, structural, and functional AA-substitution metrics, we
252 hypothesized it is also pathologically relevant. Thus, we compared glycoimpact and clinical impact for
253 ClinVar-annotated variants within 15Å, 20Å, and 30Å of UniProtKB annotated glycosites. For all three
254 distances tested, high glycoimpact (BLAMO 0.5:0.1) variants in ClinVar were robustly and significantly
255 higher (Wilcoxon p=2.6e-4, 2.2e-7, and 1.6e-10) for pathogenic variants close to glycosylation sites
256 compared to glycosite-proximal benign variants (**Figure** 5**c**). Similarly, glycoimpact is higher for likely-
257 pathogenic variants and variants of unknown significance near glycosites.

258 Examining specific ClinVar-annotated variants, we identified multiple variants in glycosylation-related
259 diseases For example, Tyrosinase:A355V (P14679) is a high-glycoimpact and glycosite-proximal causal

260 variant in oculocutaneous albinism.[48,49] While tyrosinase:A355V has not been examined for aberrant
261 glycosylation, deglycosylation disrupts tyrosinase function consistent with type 1 oculocutaneous
262 albinism.[49–53] Therefore, tyrosinase:A355V may act through aberrant glycosylation. We also observe
263 high-glycoimpact, glycosite-proximal (<30Å), pathogenic (ClinVar) variants in multiple other glycan-
264 modulated diseases including prion diseases,[54,55] lysosomal storage disorders,[56,57] and Gaucher's
265 disease.[58–61]

266 More broadly, of 1,228 non-benign ClinVar annotated variants on glycoproteins, 340 are high-
267 glycoimpact (GI>2.5) and closer than 30Å to a glycosylation site (**Table 1,** Supplementary **Table** 1**,**
268 **Supplementary Dataset 1**). This includes major diseases not typically considered related to N-
269 glycosylation including cystic fibrosis, long QT syndrome, renal cell carcinoma, acquired
270 immunodeficiency syndrome, and multiple blood coagulation factor deficiencies. Notably,
271 approximately 36% of the non-benign ClinVar-annotated glycoprotein variants we examined may be
272 impacted by aberrant glycosylation, a potentially underappreciated mechanism of pathogenesis.

273 We further analyzed glycosite proximity among causal variants in prion disease. We measured 3D
274 Euclidean min-distance from the two PrP glycosylation sites, N181 and N197, to all residues in human
275 prion protein (PrP) (including variants causing Creutzfeldt-Jakob disease (CJD)[62,63] and Gerstmann-
276 Sträussler-Scheinker disease (GSS))[64,65] (**Figure** 5a**,** Supplementary **Table** 2). CJD-causing variants were
277 approximately twice as close to glycosylation sites than the background distribution of all PrP sites (One-
278 sided Wilcoxon p=0.0003). GSS-causative variants also trend closer to glycosites (One-sided Wilcoxon
279 p=0.07) (**Figure** 5a, Supplementary **Figure** 11a-b). Low expression mutants, an indication of possible
280 aberrant glycosylation, trend closer to site N180 (One-sided Wilcoxon p=0.16) and appeared further
281 from N197 (One-sided Wilcoxon p=0.04) (Supplementary **Figure** 11c-d).

282 *Table 1 – Summary of variants by disease type where variants are high glycoimpact, close to glycosylation sites, and annotated*
283 *in ClinVar as non-benign. Each specific disease is listed followed by gene name(s) and an integer indicating the number (if larger*
284 *than 1) of variants in that gene corresponding to each specific disease. "*" indicates a multisystemic disorder.*

Cardiovascular Disorders	Ventricular tachycardia, polymorphic (*CASQ2* (2)); Arrhythmogenic right ventricular cardiomyopathy, dysplasia, hypertrophic (*DSG2* (4)); Long QT syndrome, Brugada syndrome (*KCNH2* (15) *KCNE1* (2) *KCNE2 TRHDE SCN1B* (3)); Primary pulmonary hypertension (*KCNK3*); Coronary artery disease, autosomal dominant (*LRP6*); Atrial fibrillation (*SCN3B*); Atrial septal defect 6 (*TLL1*); *Amyloidogenic transthyretin amyloidosis (*TTR* (6))
Coagulation & Hematologic Disorders	Upshaw-Schulman syndrome, Hereditary thrombotic thrombocytopenic purpura (*TTP ADAMTS13*); Platelet glycoprotein IV deficiency (*CD35*); Hereditary factor XI deficiency disease (*F11* (2)); Factor VII deficiency (*F7* (2)); Hemophilia (*F9*); Hereditary factor IX deficiency disease (*F9* (5)); Glanzmann's thrombasthenia (*ITGA2B*); Platelet-activating factor acetylhydrolase deficiency (*PLA2G7*); Thrombophilia (*PROC* (3)); Antithrombin III deficiency (*SERPINC1* (3))
Endocrine Disorders	*Serkal syndrome (*WNT4*); Familial Hypobetalipoproteinemia (*ANGPTL3*); *Hypocalciuric hypercalcemia (*CASR* (7)); Laron syndrome (*CGHR*); *Deficiency of ferroxidase (*CP* (3)); *Dopamine beta hydroxylase deficiency (*DBH*); Laron-type isolated somatotropin defect, short stature (*GHR* (3)); Isolated growth hormone deficiency (*GHRHR* (2)); Diabetes mellitus, insulin-resistant (*INSR*); Leprechaunism syndrome (*INSR*); Hypercholesterolaemia (*LDLR* (2)); Gonadotropin-independent familial sexual precocity, Leydig cell agenesis (*LHCGR* (2)); Hyperlipoproteinemia, type I (*LPL*);

	Hemochromatosis (*TFR2 HFE* (2)); *Deficiency of iodide peroxidase (*TPO* (3)); Hypothyroidism, congenital, nongoitrous (*TSHR*); *Ladd syndrome (*FGF10*)
Hearing Disorders	Nonsyndromic Hearing Loss and Deafnes (*MET*)
Immune Disorders	Cyclical neutropenia (*ELANE* (5)); X-linked severe combined immunodeficiency (*IL2RG* (2)); Severe combined immunodeficiency disease (*IL7R* (2)); Myeloperoxidase deficiency (*MPO*); Complement deficiency, C1 esterase inhibitor deficiency (*SERPING1* (2)); Acquired immunodeficiency syndrome (AIDS) (*IL4R*)
Metabolic Disorders	*Aspartylglycosaminuria (*AGA*); Infantile hypophosphatasia (*ALPL* (2)); Farber's lipogranulomatosis (*ASAH*); Pseudocholinesterase deficiency, Bche, j variant (*BCHE*); *Biotinidase deficiency (*BTD* (13)); *Combined deficiency of sialidase and beta galactosidase, Galactosialidosis (*CTSA* (2)); Ceroid lipofuscinosis, neuronal 1, 10, and 13 (*CTSF PPT1* (5) *RP11-295K3.1 CTSD* (3)); Glycogen storage disease II (*GAA*); *Gaucher disease type 1, perinatal, lethal, subacute, acute, neuronopathic (*GBA* (13)); *Fabry disease (*GLA* (4)); Tay-Sachs disease, B1 variant (*HEXA* (4)); *Sandhoff disease (*HEXB* (2)); *Hurler syndrome, Gangliosidosis, Mucopolysaccharidosis, MPS-II, MPS-IV-B, MPS-I-H/S, MPS-III-A, MPS-III-B, MPS-IV-A, MPS-VII (*ARSB* (2) *IDS* (2) *GLB1* (5) *SGSH* (2) *NAGLU GALNS* (4) *MCOLN1 GUSB* (3)); *Danon disease (*LAMP*); *Sialidosis, type II (*NEU1*); *Niemann-Pick disease type A, B, C1, Sphingomyelin/cholesterol lipidosis (*NPC1* (7) *SMPD1* (2)); Hereditary acrodermatitis enteropathica (*SLC39A4*); *Congenital disorder of glycosylation type (*STT3A MOGS*); *Multiple sulfatase deficiency (*SUMF* (2)); Crigler-Najjar syndrome (*UGT1A8 UGT1A10* (2*) UGT1A9 UGT1A7 UGT1A6* (3) *UGT1A5 UGT1A4 UGT1A3* (2) *UGT1A1* (2))
Musculoskeletal Disorders	Geleophysic dysplasia (*ADAMTSL2*); Chondrodysplasia punctata 1, X-linked recessive (*ARSE*); Orofacial cleft (*BMP4*); Spondyloepiphyseal dysplasia with congenital joint dislocations (*CHST3*); Hypochondroplasia (*FGFR3*); Bruck syndrome (*FKBP10*); Brachydactyly, type A2, fibular hypoplasia, complex brachydactyly (*GDF5* (2)); Spondylocostal dysostosis (*LFNG*); Short stature with nonspecific skeletal abnormalities (*NPR2*); Hyperphosphatasemia with bone disease (*TNFRSF11B*); Osteogenesis imperfecta (*WNT1*); *Zimmermann-Laband syndrome (*KCNH1* (3))
Neurologic Disorders	Metachromatic leukodystrophy, late-onset, late infantile (*ARSA* (4)); Holoprosencephaly (*CDON*); Myasthenic syndrome, congenital, fast-channel, slow-channel (*CHRNA1* (5)); Epilepsy, nocturnal frontal lobe, type 3 (*CHRNB2*); *Congenital muscular dystrophy, Bethlem Myopathy (*COL6A2* (4)); Febrile seizures, familial, 11 (*CPA6*); *Lipid proteinosis (*ECM1* (1)); Familial febrile seizures 8|not provided (*GABRG2*); Focal epilepsy with speech disorder with or without mental retardation (*GRIN2A* (2)); Megalencephalic leukoencephalopathy (*HEPACAM*); Episodic ataxia type 1 (*KCNA1*); X-linked hydrocephalus syndrome (*L1CAM*); Charcot-Marie-Tooth disease (*MPZ* (2)); Early infantile epileptic encephalopathy 9, 19, 32 (*PCDH19 KCNA2 GABRA1*); *Congenital muscular dystrophy-dystroglycanopathy (*POMK*); Genetic prion diseases, Jakob-Creutzfeldt disease, Gerstmann-Straussler-Scheinker syndrome (*PRNP* (6)); Progressive myoclonic epilepsy (*SCARB2*); Infantile Parkinsonism-dystonia (*SLC6A3*); Hyperekplexia (*SLC6A5*); Dystonia (*TOR1A*); Temple-Baraister syndrome (*KCNH1*)
Oncogenic	*Hereditary diffuse gastric cancer, Endometrial carcinoma (*CDH1* (2)); *Lynch syndrome (*EPCAM*); Renal cell carcinoma, papillary (*MET* (2)); *Multiple endocrine neoplasia, type 2a, type 2 (*RET* (6))
Ophthalmological Disorders	Peters anomaly (*EPHB2*); Microphthalmia (*GDF3*); Retinitis pigmentosa 68, 12, 35, Cone-rod dystrophy 10 (*SLC7A14 CRB1 SEEMA4A* (2))
Pulmonary & Gastrointestinal	*Cystic fibrosis (*CFTR* (5)); *Alpha-1-antitrypsin deficiency (*SERPINA1* (2))
Renal Disorders	Renal dysplasia (*AGT*); Diabetes insipidus, nephrogenic (*AQP2*); Nephrotic syndrome (*LAMB2*); Finnish congenital nephrotic syndrome (*NPHS1* (5)); Cystinuria (*SLC3A1*)
Rheumatologic Disorders	*Polyarteritis nodosa (*CECR1* (2)); TNF receptor-associated periodic fever syndrome (*TRAPS TNFRSF1A*)
Skin Disorders	Diffuse palmoplantar keratoderma, Bothnian type (*AQPS*); Familial progressive hyperpigmentation with or without hypopigmentation (*KITLG*); Adult junctional epidermolysis bullosa (*LAMB3*); *Kanzaki disease (*NAGA*); *Ectodermal dysplasia-syndactyly syndrome 1 (*PVRL4*); *Oculocutaneous albinism, Waardenburg syndrome, Tyrosinase-negative, Oculocutaneous albinism type 3 (*TYR* (5) *TYRP1*); Odonto Onycho Dermal dysplasia (*WNT10A*)
Vascular Disorders	*Arterial calcification of infancy (*ENPP1*); Rienhoff syndrome (*TGFB3*)

Protein structure correlates with glycan complexity in HIV gp160

To validate our predictions, we compared IMR to glycosylation on specific glycoproteins. We first found consistency between previously measured IMR (**Figure** 2**b**) and site-specific glycan complexity measurements in HIV ENV gp160 (**Figure** 6**b**).[66] PGES-DB-measured GEE-estimated IMR suggest that downstream glutamine was significantly (FDR<1e-8; OR<0.5) predictive of complexity while spatially proximal proline and lysine were weaker but significant distinguishers (FDR<1e-3, FDR<0.1 respectively, **Figure** 6**a**). As predicted, proline-proximal (within 6Å, min-distance) gp160 glycosites present more oligomannose (Two-sided Wilcoxon p=0.0033), whereas C-terminus-proximal glutamine glycosites have

293 more complex glycans (Two-sided Wilcoxon p=1e-4, **Figure** 6**c**). Spatially proximal lysine, while less
294 significant (**Figure** 6**c**), had a nonlinear impact on glycan complexity in HIV gp160; first increasing with
295 one proximal lysine then decreasing with two. The two most significant IMR predicted from PGES-DB
296 (spatially proximal proline and C-terminal glutamine) were consistent with the site-specific glycosylation
297 observed in HIV gp160.

298 IMR predict differential glycosylation on the SARS-CoV-2 spike glycoprotein

299 We also predicted glycosylation on SARS-CoV-2 spike protein S1 subunit in the ancestral strain to the
300 Gamma and Delta variants. Several of the >20 glycosylation sites[67,68] have been implicated with stability,
301 target engagement, furin cleavage, and immune evasion.[68–72] We found multiple glycosite-proximal
302 mutations within 15Å (min-distance, cubic (3D) expansion of the 6Å IMR training threshold). Gamma
303 spike S1 contains multiple mutations close to glycosylation sites including N17 (L18F, T20N, & D138Y),
304 N61 (P26S & R190S), N122 (L18F, D138Y, & R190S), N616 (D614G), and N657 (H655Y). In the Delta S1,
305 N17 and N122 have 5 and 4 proximal mutations (relative to ancestral S1), respectively, while N165 and
306 N616 each have one high-proximity mutation. Of the glycosite proximal substitutions, only L18F in
307 Gamma and F157V in Delta have a high predicted glycoimpact by IMR. L18F appears within 15Å of N17,
308 N74, N122 in Gamma. Similarly, F157V appears within 15Å of N17, N122, and N165 in Delta. High-impact
309 substitutions appear close to N17 and N122 in both variants.

310 We measured HEK293-expressed SARS-CoV-2 S1 variant glycan heterogeneity using DeGlyPHER, a mass
311 spectrometry (MS)-based glycoproteomics method,[73] to determine glycan state and occupancy at each
312 glycosylation site. We performed two independent technical replicate analyses of the S1 subunit
313 comparing Ancestral to the Gamma and Delta variants and examined 11 of the 12 canonical S1
314 glycosites (N17 was excluded due to variable signal peptide trimming). Site-specific unoccupied,
315 complex, and oligomannose/hybrid proportions were compared between variants using a Mann-
316 Whitney U test.[73] P-values were pooled across the two independent replicate analyses using the Fisher
317 method and FDR-corrected. We observed three significant differential glycosylation events (**Figure** 6**d**).
318 Complex glycans observed at N122 in Ancestral S1 were converted to more oligomannose/hybrid in
319 both Delta (oligomannose/hybrid observations increased nearly 4-fold from 13.9% in S1 to 52.5%;
320 FDR=3.3e-9) and Gamma (oligomannose/hybrid observations nearly doubled to 27.6%; FDR=7.9e-4)
321 variants. Complex glycans at N331 increased marginally from Ancestral S1 in Delta variant (from 93.7%
322 to 99.7%; FDR=0.031). Complex glycans seen at N657 in Ancestral S1 decreased in Gamma variant (by

323 over 2-fold from 53.3% to 21.1%; FDR=1.27e3). The Gamma S1 monomer was consistently expressed
324 with two novel complex glycosylation sites at N20 and N188.

325 Based on proximal high-glycoimpact substitutions, we predicted changes at N17, N74 (Gamma only),
326 N122, and N165 (Delta only). Two of four (N122 in Gamma and Delta) predicted differential
327 glycosylation events were consistent with the four observed changes (sensitivity=0.5), while 15 sites
328 where no change was predicted were consistent with the 17 sites where no change was observed
329 (specificity=0.88). This proof of concept, wherein we correctly predicted the most substantial differential
330 glycosylation event at N122 in the S1 monomer, will motivate further inspection of differential
331 glycosylation on the more physiological spike trimer and whole virus, to elucidate how differential
332 glycosylation may participate in immune evasion by SARS-CoV-2 and other viruses.

333

334 Glycosite-proximal variation in IgG sequence predicts differential Fc N-glycosylation

335 We next predicted differential glycosylation across *ighg1* missense mutation (F299I) in the IgG1 heavy
336 chain.[75] IgG1 glycosylation impacts both adaptive humoral response[76–79] and monoclonal antibody (mAb)
337 response.[80–83] Experimentally, the IgG1:F299I substitution shows a strong glycoimpact. The IgG1 variant
338 expressed in C57BL/6 and BALB/c mouse strains shows less sialylation and digalactosylation compared
339 to similarly expressed *wt* IgG1.[84–86] Additionally, BALB/c-expressed IgG1:F299I glycosylation is more
340 similar to C57BL/6-expressed IgG1:F299I glycosylation than to glycans on *wt* IgG1 expressed in the same
341 BALB/c animals (**Figure** 7**b-c**). Fc N-glycans on IgG1:F299I expressed in both BALB/c and C57BL/6 animals
342 have more agalactosylation (Mann-Whitney p=1.02e-6), less digalactosylation, and less mono-, di- and
343 total sialylation (Mann-Whitney p<0.0073) compared to *wt* IgG1 expressed in the same animals (**Figure**
344 7**c**, Supplementary **Table** 3). The increase in galactosylation in *wt* IgG1:F299 is consistent with PGES-DB
345 predicted IMR for upstream (N-terminal) phenylalanine (**Figure** 7**a**). Upstream phenylalanine is
346 associated with increased di-galactosylated biantennary structures (OR>2), while upstream isoleucine is
347 associated with tetraantennary galactosylation. Since only biantennary structures are generally
348 permitted on IgG, the galactose-promoting function of upstream isoleucine should be unrealized in this
349 glycoprotein. The increased sialylation in *wt* IgG1:F299 is also consistent with PGES-DB IMR which show
350 an association between structurally proximal phenylalanine and disialylated structures (OR>10). These
351 results suggest that glycoimpact can accurately predict several specific glycan epitopes.

352 ## Core-fucose preference is associated with percent fucosylation and high-ADCC

353 To further demonstrate IMR accuracy and functional importance, we compared predicted core-fucose
354 preference to observed fucosylation abundance and ADCC in a Fab-constant Fc-variant antibody panel[74]
355 (**Figure** 7**d-e**). Core-fucose preference was calculated as the preference of variant compared to the wild
356 type for N-glycan core motif with or without a core fucose, i.e., Man(b1-4)GlcNAc(b1-4)[Fuc(a1-
357 6)]GlcNAc(b1-4)-Asn and Man(b1-4)GlcNAc(b1-4)GlcNAc(b1-4)-Asn, respectively (see **Methods**).

358 We compared core-fucose preference for Fc-variant glycosylation on a surface-binding *Mycobacterium*
359 *tuberculosis*-specific monoclonal antibody (clone 24c5) to demonstrate the accuracy of IMR-based
360 predictions. We determined core-fucose preference predicted from GEE-derived IMR (see **Methods**) for
361 multiple Fc-variants. We then compared predicted core-fucose preference to the capillary
362 electrophoresis measured relative abundance of fucosylated glycans. The Fc-variants naturally stratified
363 into fucose-saturated (fucosylated glycans > 90%) and unsaturated variants (Supplementary **Figure** 16).
364 Fucose saturated variants showed no significant association with predicted fucose preference. However,
365 fucose-unsaturated variants alone (**Figure** 7**d**) show a strong correlation between predicted core-fucose
366 preference and percent fucosylation (R=0.9, p=0.013). 24c5 Fc glycosylation profiles therefore
367 demonstrate another instance of glycan predictability.

368 To determine if predicted changes in glycosylation can also predict glycan-modulated behaviors, we
369 examined our ability to predict increases in antibody-dependent cellular cytotoxicity (ADCC) from
370 predicted decreases in core-fucosylation, a well-characterized property of therapeutic antibodies.[83] We
371 identified 10 glycosite-proximal variants (**Figure** 7**e**) from the REFORM Fc variant panel[74] and stratified
372 the ADCC-enhancing variants from those associated with no change in ADCC. Of the five sequence-
373 proximal variants, the non-enhancing variant (T307A) shows a positive preference for core-fucose while
374 all four ADCC associated variants have a negative core-fucose preference. Among spatially proximal
375 variants, several substitutions occur in multiple variants and are not uniquely associated with ADCC
376 enhancement or non-enhancement (greyed out, **Figure** 7**e**). Of the two-remaining spatially proximal
377 variants, the non-enhancing variant (L235A) shows a positive preference for core-fucose while the ADCC
378 associated variant (G236A) has a negative core-fucose preference. These ADCC associations with core-
379 fucose preference are consistent with percent fucosylation in 24c5 Fc. T307A and L235A are highly
380 fucosylated in 24c5, predicted to prefer core-fucose, and do not enhance ADCC. Conversely, S298A is
381 least fucosylated in 24c5, shows a negative preference for core-fucose, and is associated with ADCC

382 enhancement. Our predictions therefore recapitulate the immunological implications of allotype-driven
383 differential glycosylation.

384 Discussion

385 Here, we have identified constraints on glycan biosynthesis through the analysis of site-specific protein
386 features[36] and glycan substructures.[35] With our Protein-Glycan Enriched Structure Database (PGES-DB),
387 we enumerated and quantified intermolecular relations (IMR) between protein and glycan structure in
388 human glycoproteins. We then computed the expected differential glycosylation, the "glycoimpact,"
389 associated with specific protein structure changes. We validated glycoimpact importance by comparison
390 to substitution matrices, evolutionary couplings, and pathogenicity scores. We further examined
391 glycoimpact sensitivity and specificity comparing predictions with observed glycosylation on PrP, HIV
392 gp160, and IgG glycoproteins. The existence and utility of glycoimpact suggests that glycans are not
393 synthesized template-free. Rather, the glycoprotein surface constrains glycan biosynthesis, deciding
394 which glycosyltransferases may dock and continue glycosylation. Thus, glycosylation is a bounded
395 biosynthesis wherein a range of glycans within biosynthetic pathways are requested through local
396 glycosite structural constraints (likely dictated by glycoprotein-glycosyltransferase docking feasibility)
397 and those requests are variably fulfilled given metabolic precursor-availability.

398 The significant associations between glycan and protein structures seen in PGES-DB is not consistent
399 with the expected independence if glycan biosynthesis was template-free. Instead, it suggests protein
400 structure provides substantial information regarding glycan structure. However, the observation that
401 larger glycans are less determined by protein structure supports precursor-limitations of bounded
402 biosynthesis, wherein larger glycans require more precursors, any of which can limit fulfillment.
403 Similarly, low fulfillment is seen in high-yield expression systems[87] necessitating, in some cases,
404 supplementation with maturing glycoenzymes.[88–90]

405 Our quantified protein-glycan IMR describe an expanded glycosite structure, beyond the original sequon
406 definition (NX[S/T]).[5] We discovered many new sequence-proximal AA IMR both upstream and
407 downstream of traditional glycosites. The enhanced aromatic sequon (EAS)[14] corroborates one such
408 sequon-expanding IMR. Upstream phenylalanine IMR predicts an increase in Man7 structures (i.e., N-
409 glycan with seven-mannoses) and a decrease in Man6 structures, suggesting an increase in larger high-
410 mannose structures (**Figure** 3**d**). The predicted difference in oligomannose is consistent with reported
411 EAS glycosylation; upstream phenylalanine (N-2) can decrease glycan processing and increase
412 homogeneity.[14] Structurally, tryptophan and tyrosine are known to stabilize the chitobiose core through

413 dispersion and increasing glycan accessibility for maturation; phenylalanine lacks a dipole and therefore
414 does not support similar maturation[91–95]. Both the EAS and selective aromatic stacking results are
415 consistent with glycoimpact. We predict limited expected differential glycosylation following a
416 tryptophan-tyrosine substitution but a substantial decrease in processing following substitution from
417 tryptophan or tyrosine to phenylalanine (**Figure** 3**f**, Supplementary **Figure** 5). The expanded sequon
418 scaffolded by the IMR (**Figure** 2), glycoimpact substitution matrix (**Figure** 3**f**, Supplementary **Figure** 5),
419 and glycosite-coupled residues (**Figure** 4**c-d**) together represent a portable and dynamic summary of our
420 findings that can be easily applied to predict glycosylation following novel substitutions. We believe that
421 the large number of both high glycoimpact and low structural impact substitutions (around 50% of AA
422 have one such substitution) will be useful in understanding pathogenic variants, viral evolution, and
423 glycoprotein engineering.

424 Glycoimpact can be further used to inform the mechanism of pathogenesis when disease variants are
425 close to glycosites that impact glycosylation. We can examine known annotated-pathogenic variants and
426 propose novel mechanisms of pathogenesis. Unannotated variants can be automatically labelled for
427 likelihood of glycan modulation. Though this work does not deeply interrogate causal associations with
428 glycan-modulated pathogenesis, we found several prior works implicating high-glycoimpact glycosite
429 proximal variants as pathogenic, including one thorough study of oculocutaneous albinism implicating
430 variant-proximal glycosylation as a causal pathogenic modulator. Examining the highest glycoimpact
431 relation with a high BLOSUM score, Ile/Val; the substitution should have a negligible structural impact
432 while dramatically changing glycosylation. As expected, pathogenic variant PrP:V180I (adjacent to
433 glycosite N181) is a causal mutation in Creutzfeldt-Jakob disease.[96] Similarly, a glycosite-proximal V84I
434 substitution in HIV-gp120 deactivates the virus; otherwise achieved by mutagenic glycosite-ablation.[97]
435 Similarly, tyrosinase:A355V (P14679) is a sufficient cause of oculocutaneous albinism.[48,49] A355V is also a
436 high glycoimpact variant and close to the function-critical N371 glycosite (<20Å; PDB:5M8N); tyrosinase
437 glycosylation is critical for proper folding,[51,98] N371 glycosite ablation results in decreased protein
438 abundance and activity,[99] and non-mutagenic post-expression tyrosinase deglycosylation also interrupts
439 function.[53] Using glycoimpact, we can propose A335V as a glycan-based mechanism of pathogenicity.
440 Beyond tyrosinase, we identified thousands of variants across hundreds of diseases that may be
441 similarly explained by aberrant glycosylation. There may be millions of high glycoimpact variants close to
442 glycosites beyond the narrow scope of ClinVar annotation for which glycoimpact can suggest a possible
443 pathogenic mechanism.

444 Just as amino acid substitution can assert pathogenic glycosylation on human proteins, similar
445 substitutions can enable immune evasion for viruses. Consistent with glycoimpact predictions, we show
446 that glycosite proximal proline and glutamine are associated with glycan complexity across HIV gp160.
447 These results both validate our model and propose mechanisms for evolutionary control over the viral
448 glycan shield.[11,25,100,101] Across three SARS-CoV-2 Variants of Concern, we show that high glycoimpact
449 variations close to glycosites produce IMR-consistent differential spike glycosylation. If IMR can predict
450 differential glycosylation as viruses evolve, these predictions could help predict immune evasion and
451 predict the viral evolutionary landscape for many viruses.[11,101,102]

452 Functional differential glycosylation is also critical in protein therapeutics. Glycoengineering for
453 therapeutics is often costly, application specific, and siloed from protein design. Glycans can be modified
454 indirectly through genome editing of glycosyltransferases[103–105] or media optimization,[106–108] and such
455 strategies can be guided by models of the biosynthetic pathways.[109–114] Here, we examined AA-specific
456 differential glycosylation events on antibodies. On the previously characterized and differentially
457 glycosylated mouse IgG1 allotype (I299F), we see IMR-predictable glycosylation encoded directly into
458 the glycoprotein primary sequence. Similarly, in glycosite-proximal and high glycoimpact mAb-Fc-
459 variants both fucosylation and fucose-modulated functional response (ADCC) correlated with GEE-IMR
460 core-fucose preference. In these examples, IMR is a biologically[76–78] and therapeutically[74,115–118] useful
461 method for connecting allotype, glycosylation, and effector function. Therefore, IMR represent an
462 opportunity to embed glycoengineering directly into the glycoprotein sequence and combine the
463 currently separate paradigms of glycoengineering and protein engineering to a unified practice of
464 glycoprotein engineering: considering the structure of both protein and glycan and their mutual
465 influence.

466 Our direct results focus on human-expressed glycoproteins and global trends rather than specific
467 mechanisms such as aromatic chemistry, or chaperone proteins. While the specific glycoimpact trends
468 may not extend to other organisms, the chemistry of carbohydrate-protein interactions suggest that
469 glycoimpact is foundational and therefore exists in some form across glycosylated proteins.

470 We believe the evidence presented demonstrates the utility of glycoimpact. Further, the predictability
471 of glycosylation from protein structure demonstrates that glycosylation is a genetically-encoded
472 bounded biosynthesis. Due to the high degree of accuracy, precision, and reproducibility with which
473 protein structure appears to bound glycosylation, we believe protein structure may be described as a
474 template for glycan biosynthesis. Predictability in glycobiology from such templates will unlock a wealth

475 of theoretical, exploratory, and corroborative analysis making it inexpensive and easy to leverage
476 glycobiological insights in fields throughout biology.

477

478 Conclusions

479 Our results are incompatible with the template-free principle of glycan biosynthesis. Glycoimpact,
480 defined and validated here, presents a metric for estimating the influence of a protein structure on
481 glycosylation. The evidence presented asserts that once the precursor-limitations of biosynthesis are
482 considered, protein structure influence on glycans becomes visible. Because precursor-limitations are a
483 substantial force in glycan biosynthesis, protein structure describes a less obvious mapping than
484 canonical templates such as DNA, RNA, or protein biosynthesis. It is nonetheless predictable, accurate,
485 and reproducible within a requested range of permissible glycans.

486 Notably, bounded biosynthesis, imposed through local protein structural constraints, is not a behavior
487 unique to glycans. Within biology there are likely other cases of biosynthesis or modification constrained
488 or directed by local protein structure. Because molecules exist in physical space and possess chemical
489 properties, both the target molecules and the modifying proteins may influence each other by
490 generalizable steric and chemical interactions between their surfaces. Other target-modifier relations
491 likely exist in similar interactions such as chromatin and epigenetic modification (e.g. neither histone
492 deacetylases nor chromatin demethylases uniformly impact accessible chromatin),[119] post-translational
493 modification,[120,121] and RNA-binding protein actuated splicing.[122–124] Any instance involving a target
494 molecule placed in distinct local protein structures modified by a small set of enzymes could be an
495 instance of bounded biosynthesis.

496

497 Acknowledgements

498 Thank you to Terry Platt who inspired me with tales of the *Trp* operon[125–129] and in doing so planted the
499 seed of thought that substrate-limitation is not mutually exclusive with templated biosynthesis. Thanks
500 also to Lorenzo Casalino, Christian Seitz, and Rommie Amaro for their early insights into the project in
501 the context of influenza glycoprotein structure. We would like to acknowledge the invaluable
502 contribution of Dr. Jasminka Krištić, Prof. Dr. Grant Morahan and Prof. Dr. Falk Nimmerjahn to the
503 studies of IgG N-glycome that are referred to in this paper. EA is supported by ANID (DOCTORADO
504 BECAS CHILE/2018 - 72190270), the Fulbright Chile Commission, and the Siebel Scholar Foundation. This

work was supported by NIGMS (R35 GM119850, NEL) and the Novo Nordisk Foundation (NNF20SA0066621, NEL).

Conflicts

This work is associated with a provisional patent filed by the authors, and Augment Biologics, founded by BK and NEL.

Methods

Enrichment of glycan-protein site-matched data to generate the Protein-Glycan Enriched Structure Database (**PGES-DB**)

Starting from site-specific glycosylation events, we extended the annotation of each glycosylation site and glycan to include detailed site-specific protein structural annotation and recorded the number of times each substructure appeared in each glycan. Only human glycoproteins were analyzed. The final database includes 111 proteins, 306 glycosylation sites and 4,263 glycans. We initially used site-specific glycosylation events documented in UniCarbKB.[38] Later and current work was informed by glycosylation events documented in GlyConnect[130] with supplemental information from GlyGen.[131] Empirical and expert-curated site-specific glycosylation events from the UniCarbKB and GlyConnect were used to inform much of the core analysis. Glycoprofiles from UniCarbKB were collected from GlycosuiteDB,[132] EUROCarbDB,[133] and expanded meta-analysis data.[24] GlyConnect glycoprofiles were predominantly (70%) curated from novel experiments but includes GlycosuiteDB[132], and select large scale studies.

The protein structure annotation was done using the Structural Systems Biology (ssbio) package in python.[36] The package uses several tools to perform a variety of annotations. For each human protein, empirical and homology modeled structures were collected from the Protein Data Bank (PDB)[134] and SWISMOD,[135] respectively. Proteins without existing models were modelled using I-TASSER.[136] Protein structures and chemistry close to the glycosylation sites were annotated multiple software packages through ssbio: sequence properties (EMBOS:*pepstats*),[137] sequence alignment (EMBOS:*needle*),[137] secondary structure (DSSP,[138] SCRATCH::SSpro[139] and SCRATCH::SSpro8), solvent accessibility (DSSP and FreeSASA), and residue depth (MSMS). Additional amino acid aggregate features were calculated using

533 R::seqinr. Spatial proximity was defined using "min-distance" between two amino acids; the minimum
534 distance between any pair of atoms spanning the amino acids.

535 Glycan structures were annotated using a combination of glypy[140] and GlyCompare[35] for structure
536 parsing and comparison respectively. All glycan substructures, a connected subset of monosaccharides
537 with and without linkage information, were extracted from each glycan, merged to make a superset of
538 substructures, then mapped to each glycan. Thus, resulting in a mapping from every glycan in the input
539 database to shared substructures.

540

541 Software and packages

542 Protein structure analysis was performed in Python v2.7.15 using ssbio v0.9.9.8 to retrieve and
543 calculate: existing empirical and homology models from PDB and SWISSMOD (PDBe SIFTS),[141] *de novo*
544 homology models (I-TASSER v5.1), sequence properties (EMBOS v6.6.0.0 pepstats), sequence
545 alignment(EMBOS v6.6.0.0 needle), secondary structure (DSSP v3.0.0, SCRATCHv1.1::SSpro and
546 SCRATCHv1.1::SSpro8), solvent accessibility (DSSPv3.0.0 and FreeSASAv2.0.2), and residue depth
547 (MSMSv2.2.6.1). Additional amino acid aggregate features were calculated using R::seqinr.

548 Statistical analysis was performed in R v3.6.1. R::entropy v1.2.1 was used for entropy, Kullback-Leibler
549 divergence and other information theoretic calculations. Generalized Estimating Equations (GEE) were
550 fit using R::geepack v1.3.1. Gaussian Mixture Models were used to z-score normalize the glycoimpact
551 using R::mixtools v1.1.0. BLOSUM and PAM substitution matrixes were accessed from R::Biostrings
552 v2.52.

553 Probability event space, information gain and conditional probability

554 Here we define an event (a row in our enriched glycosylation-glycosite database) as "the observation of
555 a glycan at a glycosylation site in an experiment." If two separate experiments in the input database
556 both observe the same glycan at the same site on the same protein, we consider that event to have
557 occurred twice. Within each event, we ask if the glycan structure random variable (the presence or
558 absence of a specific glycan substructure) is present or absent in the observed glycosylation event and if
559 the protein structure random variable (a proximal amino acid, a secondary structure or another discrete
560 protein structure). A Fisher exact test (R::base::fisher.test) was used to estimate the odds ratio (OR) and
561 significance (p) of each inter-molecular relation (IMR). P-values were corrected for False Discovery Rate
562 (FDR, q) permitting 10% false discovery ($q<0.1$). Conditional probability was calculated by dividing joint

563 probability by the marginal probability of protein and glycan structure presence. Kullback-Leibler
564 divergence (KLd, R::entropy::KL.Dirichlet, pseudo count=1/6) was calculated by comparing the
565 conditional probability distribution to the marginal probability distributions.

566 Quantitative characterization of Inter-Molecular Relations (IMR) using Generalized Estimation 567 Equations (GEE)

568 To characterize the IMR in the PGES-DB while controlling for protein-specific confounding effects and
569 handle nonlinear relations we used a population-averaging approach; logistic Generalized Estimating
570 Equations (GEE) with glycoprotein identity as the cluster identifier.[142] We used an exchangeable
571 correlation structure to describe and balance the in-protein similarity. Models were fit to predict glycan
572 substructure binary (presence or absence) from either z-score normalized continuous or binary
573 (presence or absence) protein structures. For each model, the data from PGES-DB was isolated for one
574 glycan-type (N-glycan or O-glycan), one glycan substructure and one protein structure. Incomplete
575 observations (events/rows) were removed and then several checks on each data-slice were run to
576 minimize overfitting. Glycan substructures were excluded from modelling if standard deviation was less
577 than 1e-6 or if there were fewer than 5 observations of the structure within the pertinent data-slice.
578 Discrete protein structure features were excluded if there were fewer than 4 observations within the
579 data-slice. Models were excluded if there were fewer than 4 instances in any cell (of the 2x2
580 absence/occurrence matrix) or if the chi-squared expected value of any cell was less than or equal to 5.
581 Observations were weighted by the reciprocal-count of the corresponding label type to balance label
582 contributions to the model and scaled by exponentiated cscore to maximize the contribution of high-
583 quality protein structure models ($w_i = 2^c / n$); c is the c-score given by I-TASSER and n is the number of
584 times a structure is present (1) or absent (0). Models with $|\log(OR)| > 50$ were excluded as likely overfit.
585 Quasi-likelihood under independent model criterion (QIC) and the Wald tests were used to evaluate the
586 significance and magnitude of the estimated IMR. We also ran this analysis using publication identifiers
587 as a control variable to account for researcher and group biases; this produced similar results likely
588 because protein identity is strongly correlated with the publications in which they appear.

589 Calculating glycoimpact from IMR and populating a BLAMO matrix

590 Glycoimpact is the z-score normalized Euclidean distance between the significant log(OR) for all motifs
591 associated with a protein structure; the null distribution of Euclidean distances was determined using
592 Gaussian mixture models (Supplementary **Figure** 5)

593 Glycoimpact is calculated for every pair of AAs as the Euclidean distance between significant and
594 substantial log odds ratios for each AA; the Euclidean distance between expected glycoprofiles for each
595 AA. The substantial (log(OR)>X) and significant (FDR<Y) log(OR) values are retained while insignificant or
596 unsubstantial log(OR) values are set to zero. The resulting matrix describes the expected glycoimpact
597 due to each AA-substitution, termed the BLAMO XY matrix where X and Y denote the log(OR) and FDR
598 thresholds respectively.

599 Glycoimpact values from a BLAMO XY matrix can then be z-score normalized to a Gaussian Mixture
600 Model[143] estimated null distribution. We use z=2.5 as a heuristic but stringent cutoff between
601 "impactful" (z>2.5) and "null" (z<2.5) substitutions.

602 Comparison of SNP pathogenicity scores with glycoimpact

603 Functional prediction rank normalized scores were obtained from dbNSFP (v3.2) for the following 27
604 tools: SIFT, PolyPhen-2 HDIV, PolyPhen-2 HVAR, GERP++, MutationTaster, Mutation Assessor, FATHMM,
605 LRT, SiPhy, 2x PhyloP, MetaSVM, MetaLR, CADD, VEST3, PROVEAN, 4× fitCons scores, fathmm-MKL,
606 DANN, 2× phastCons, GenoCanyon, Eigen and Eigen-PC.[40] Variants were excluded from the analysis if
607 they had more than 3 missing functional score predictions, did not result in an amino acid change, or not
608 on proteins that had known glycosylation sites.

609 Assignments of "prediction-type" and "structure-usage" (**Figure** 5b) were adapted from classifications
610 provided by dbNSFP.[40]

611 Estimation and Analysis of Evolutionary Couplings (EC)

612 For EVCouplings calculation, hits composed of more than 50% gaps were filtered from the alignment,
613 and sequences with homologs more than 80% identical were down-weighted to compute N_{eff}, the
614 effective number of sequences.[45] ECs were calculated using pseudo-likelihood maximization,[144,145] as
615 implemented previously.[146] The λ_J term was scaled by the number of amino acids minus one times the
616 number of sites in the model minus one. Pre- and post-processing was performed using the EVCouplings
617 Python package.[147]

618 High-ranking EC events are generally considered those ranking less than *L* a measure of sequence length
619 where only residues with fewer than 30% gaps were counted.[45] Specifically, the gap threshold (minimum
620 column coverage parameter) was set to 70%. Therefore, residue positions with more than 30% gaps
621 disregarded. We also used a fragment filter of 70%, meaning that individual sequences had to have 30%
622 non-gap characters in each row as well. We explored multiple high-rank thresholds between *L/5* and *3L*.

623 To explore the increased coupling with glycosylation sites, we examined couplings between each amino
624 acid with glycosites (GN), asparagines (N) and any amino acid (AA). We compared the number of high-
625 ranking coupling events, the distributions of EC probabilities and the relative numbers of high and low-
626 ranking ECs for each group with various amino acids at relative positions N+/-6. Distributions were
627 compared with a one-sided Wilcoxon test and high/low-ranking counts were compared with
628 hypergeometric enrichment. The hypergeometric enrichment of glycosite-coupling was performed at
629 multiple high-rank thresholds (*L/3, L/2, L, 2L, 3L*) and p-values were pooled for each amino acid at each
630 relative position across ranks using Fisher's method. Finally, the pooled p-values were corrected for
631 multiple tests using the Benjamini-Hotchberg method.

632 To examine larger structures in ECs, we used EC rank to mask extended sequons (N+/-6) then clustered
633 the sequons and extracted motifs. For each sequon, the residues were retained if the residue-glycosite
634 coupling rank was less than *L4*. The extended and masked sequons were distinguished using a hamming
635 distance (DECIPHERv2.18.1)[148] then clustered using agglomerative hierarchical clustering
636 (factoextra::hcut v1.0.7). Motif logos were generated using custom-scaled position-specific scoring
637 matrices[149] reflecting the cumulative rank of amino acids at each glyco-site relative position. Specifically,
638 the aggregate score, *S,* for each amino acid, *a*, at each position, *p*, was aggregated over EC score ranks, *r,*
639 within each extended-masked sequons, *s*, in a cluster, *c*, such that $S_{a,p} = log_{10}\left(\sum_{s \in c} \quad L/r\right)$

640 ## Mouse breeding and Samples

641 The Collaborative Cross (CC) recombinant inbred mouse strains (N = 333, 95 strains, age 20-117 weeks)
642 were produced by Geniad Pty Ltd and housed at Animal Resources Centre (Murdoch, WA, Australia).[150]
643 The CC strains were genotyped using the MegaMUGA platform (GeneSeek; Lincoln, NE). C57BL/6 (N =
644 10) and BALB/c mice (N = 10), sex- and age-matched (10 weeks old, 1:1 male:female) were obtained
645 from Elevage Janvier (Le Genest-Saint-Isle, France).[86] The studies received appropriate ethics approvals
646 from the Animal Ethics Committee of the Animal Resources Centre[75] and the Ethical Committee of the
647 District Government of Lower Franconia.[86]

648 ## Liquid Chromatography – Mass Spectrometry (LC-MS), Normalization and Statistical Analysis of
649 Mouse Fc-linked IgG N-glycopeptides

650 Immunoglobulin G was isolated from 100-500 µl of mouse serum on 96-well Protein G monolithic plates
651 (BIA Separations) as described previously.[75,85] LC-MS analysis of tryptic Fc-glycopeptides was performed
652 as described in.[75,85] In brief, approximately 10–20 µg of isolated IgG was digested with 200 ng trypsin

653 (Worthington, USA). The resulting glycopeptides were purified by reverse-phase solid phase extraction
654 using Chromabond C18ec beads (Marcherey-Nagel, Germany) as described in.[85] Tryptic digests were
655 analyzed on a nanoACQUITY UPLC system (Waters, USA) coupled to a Compact mass spectrometer
656 (Bruker Daltonics, Germany). Peak areas were calculated by summing areas for doubly and triply
657 charged ions determined with LaCyTools v 1.0.1 b.7 software[151] and normalized to the total integrated
658 area per IgG subclass.

659 Batch correction was performed on the log-transformed values using the ComBat method (R package
660 "sva") to remove possible experimental variations due to LC-MS analysis having been performed on
661 several 96-well plates within each cohort. Derived glycosylation traits describing relative abundance of
662 N-glycans sharing specific structural features (agalactosylated, galactosylated, sialylated,
663 monogalactosylated, digalactosylated, monosialylated, disialylated structures, structures with bisecting
664 GlcNAc) were calculated in a subclass-specific manner.[86] Statistical analysis and data visualization were
665 performed using R programming language v 4.0.3.

666 Glycoproteomics for SARS-CoV-2 Spike glycoproteins

667 His-tagged recombinant SARS-CoV-2 Spike S1 protein, expressed in HEK293 cells were purchased from
668 Sino Biologics (Wayne, PA). Lyophilized glycoproteins corresponding to the original 2019 strain (40591-
669 V08H), the Gamma variant (40591-V08H14 with L18F, T20N, P26S, D138Y, R190S, K417T, E484K, N501Y,
670 D614G and H655Y mutations), and the Delta variant (40591-V08H23 with T19R, G142D, E156G, 157-158
671 deletion, L452R, T478K, D614G and P681R mutations). Samples were analyzed using DeGlyPHER.[73]

672 Briefly, glycoproteins were digested with Proteinase K (30 min or 4 h) or trypsin, sequentially
673 deglycosylated with Endo H (creating residual mass signature of +203 Da) to signify high
674 mannose/hybrid glycans, and then with PNGase F in $H_2{}^{18}O$ (creating residual mass signature of +3 Da) to
675 signify the remnant complex glycans on any sequon (NXS|T, where X is any amino acid except P)
676 asparagine. Unoccupied sequons will have no additional signature mass. Analysis of samples was done
677 on a Q Exactive HF-X mass spectrometer (Thermo), injecting directly onto a 25 cm, 100 µm ID column
678 packed with BEH 1.7 µm C18 resin (Waters). Liquid chromatography separation was achieved at a flow
679 rate of 300 nL min−1 on an EASY-nLC 1200 (Thermo). Buffers A and B were 0.1% formic acid in 5 and
680 80% acetonitrile, respectively. The gradient used was 1–25% B over 160 min, an increase to 40% B over
681 40 min, an increase to 90% B over another 10 and 30 min at 90% B for a total run time of 240 min. The
682 column was re-equilibrated with solution A before injecting sample. Peptides eluting from the tip of the
683 column were nanosprayed directly into the mass spectrometer by application of 2.8 kV at the back of

684 the column. The mass spectrometer was operated in a data-dependent mode. Full MS1 scans were
685 collected in the Orbitrap at 120000 resolution. The 10 most abundant ions per scan were selected for
686 HCD MS/MS at 25 NCE. Dynamic exclusion was enabled with a 10 s duration and +1 ions were excluded.
687 Peptides were identified with Integrated Proteomics Pipeline (IP2, Bruker Scientific LLC). Tandem mass
688 spectra were extracted from raw files using RawConverter[152] and searched with ProLuCID[153] against a
689 database comprising UniProt reviewed proteome for Homo sapiens (UP000005640), including additional
690 UniProt amino acid sequences for Endo H (P04067), PNGase F (Q9XBM8), and Proteinase K (P06873), the
691 amino acid sequences for the SARS-CoV-2 S1 subunits, and a list of general protein contaminants. The
692 search included no protease specificity (all fully tryptic and semitryptic peptide candidates when treated
693 with trypsin). Carbamidomethylation (+57.02146 C) was used as a static modification. Deamidation in
694 the presence of $H_2{}^{18}O$ (+2.988261 N), GlcNAc (+203.079373 N), oxidation (+15.994915 M), and N-
695 terminal pyroglutamate formation (−17.026549 Q) were used as differential modifications. Data were
696 searched with 50 ppm parent mass tolerance and 50 ppm fragment mass tolerance. Identified proteins
697 were filtered using DTASelect2[154] while using a target-decoy database search strategy to limit the false
698 discovery rate to 1%, at the spectrum level.[155] At least one peptide per protein and no tryptic end (or
699 one tryptic end when treated with trypsin) per peptide were necessary, and precursor delta mass cutoff
700 was fixed at 10 ppm. Statistical models for peptide mass modification (modstat) were applied (trypstat
701 was additionally applied for trypsin-treated samples). Semi-quantitative label-free analysis was
702 performed based on the precursor peak area, with a 10 ppm parent mass tolerance and 0.1 min
703 retention time tolerance, Census2.[156] "Match between runs" was used to find missing peptides between
704 runs. GlycoMSQuant (v.1.4.1, https://github.com/proteomicsyates/GlycoMSQuant)[73] was used,
705 summing precursor peak areas across the 3 conditions – 30 min and 4 h Proteinase K, and trypsin,
706 discarded peptides without glycosites, and discarded misidentified peptides when N-glycan remnant
707 mass modifications were localized to non-glycosite asparagines and corrected/fixed N-glycan
708 mislocalization where appropriate, to finally calculate proportions of 3 glycosylation states at each
709 glycosite, with +/-SEM (standard error of mean). Pairwise statistical comparison between variants was
710 performed using Mann-Whitney U Test.

711 The entire DeGlyPHER pipeline and measurement were run twice to collect two independent technical
712 replicates. Using the Fisher's method for pooling independent p-values, we combined the Mann-
713 Whitney U-derived p-values for each glycosite comparison. Pooled p-values were adjusted for multiple-
714 testing using FDR. The N17 glycosite was inconsistently cleaved with the signal peptide precluding stable
715 measurements needed for robust comparison.

716 ## Estimation of glycomotif preference from IMR

717 Here, we define glycomotif (e.g., core-fucose) preference. Briefly, this is the preference for a glycomotif
718 following a substitution compared to the wildtype (WT) and a close (within one monosaccharide)
719 precursor of the glycomotif of interest. When the IMR relating the lost (WT, x-axis) and gained (variant,
720 y-axis) amino acids association (IMR) to the glycomotif and glycomotif precursor, the variant preference
721 can be calculated as the distance between the glycomotif and glycomotif-precursor points; distance is
722 the component perpendicular to the line of equity (y=x). Supplementary **Figure** 15 demonstrates this
723 calculation visually.

724 Glycomotif preference can be described in more precise terms. Given a substitution where X and $Y$are
725 WT and mutant amino acids respectively at an amino acid residue at index I, we may describe the
726 substitution as XIY. When I is glycosite-proximal, we may describe a substitution, XIY, as a point, p,
727 with a pair of IMR (ρ) relating each amino acid to a single glycomotif, $p_{XIY} = (\rho_X, \rho_Y)$. The IMR-pair,
728 $p_{XIY} = (\rho_X, \rho_Y)$, may also be described as a vector terminating on that point, $\vec{p}_{XIY}$. We may also
729 represent the line of equality ($y = x$) by the normalized vector $\vec{n} = \left(\frac{1}{\sqrt{2}}, \frac{1}{\sqrt{2}}\right)$. Here, the glycoimpact is
730 the minimum distance, $G = d(\vec{p}, \vec{n})$. To calculate the component of $\vec{p}$ parallel to $\vec{n}$, we project $\vec{p}$ onto $\vec{n}$,
731 $\vec{p}_{\vec{n}} = \frac{\vec{p} \cdot \vec{n}}{\vec{n} \cdot \vec{n}} \cdot \vec{n}$. Therefore, $G = d(\vec{p}, \vec{n}) = \vec{p} - \vec{p}_{\vec{n}}$

732 With this definition of G, we can define G_i and G_c as the glycoimpact corresponding to the glycomotif of
733 interest and the contract glycomotif respectively. Then, the relative preference by first calculating the
734 perpendicular component of the difference in glycoimpact vectors projected onto $\vec{n}$, such that
735 $r_{\vec{n}} = (G_i - G_c)_{\vec{n}}$. Then R is the l^2-norm of the vector difference, $R = s|r_{\vec{n}}|$. For $r_{\vec{n}} = \langle x, y \rangle$, we define
736 the sign, s, as positive if $y > x$ and negative if $x > y$. The sign is not defined if $x = y$.

737 ## Glycoprofiling of 25c4 monoclonal antibody using capillary electrophoresis

738 As was recently described,[157] 54 Fc variants of 25c4 were cloned from the REFORM Fc variant panel.[74]
739 The REFORM plasmid library[74] is comprised of golden gate cloning plasmids[158] with BsaI restriction sites
740 flanking distinct antibody domains and a furin 2A cleavage site to enable self-cleavage and successful
741 assembly of a complete antibody from a single open reading frame.[159] Variable Light chains containing
742 REFORM variants and 25c4 Variable Heavy chains were simultaneously transfected at a 1:1 ratio in CHO
743 cells, purified using a Protein A chromatography resin, then dialyzed and concentrated with Phosphate
744 Saline Buffer (PBS).

745 Fc glycosylation was then measured on purified 25c4 antibodies. Purified antibodies were incubated
746 with magnetic G protein beads (Millipore) and separated from Fab fragments following enzymatic
747 digestion (IdeZ, NEB). Fc glycans were released and labelled using the GlycanAssure ATPS kit (Thermo
748 Fisher Scientific) then separated using 3500xL Genetic Analyzer (Thermo Fisher Scientific). As previously
749 described,[160] retention times (RT) were matched to glycan standards using Glycan Acquisition Software
750 Version 3500 v1.0.3 and Glycan Analysis Software v1.1. Abundance (area under peaks) was normalized
751 to total area per sample to calculate relative abundance of each glycan. Non-uniquely determined
752 glycans were excluded (where the difference in RT was below the detection threshold).

753
754

755

Figure Captions

Figure 1 – DNA, RNA, and protein biosynthesis are template-driven processes. Glycan biosynthesis is believed to be non-templated and regulated by metabolic and enzymatic constraints. Here we explore protein structure influence on glycan biosynthesis. In our theory of "bounded biosynthesis", the glycoprotein (black) surface requests glycans by permitting specific glycosyltransferases (blue and yellow) to dock and the metabolic and enzymatic constraints govern the extent to which those requests are fulfilled. Therefore, we posit that glycan biosynthesis is accurately and reproducibly constrained by protein structure; an effect visible after accounting for metabolic influence. Glycans are represented using IUPAC-extension for glycans and the Symbol Nomenclature for Glycans (SNFG[1,2]); Mannose (Man), Galactose (Gal), Sialic Acid (Neu5Ac), N-Acetylglucosamine (GlcNAc), Fucose (Fuc). Here, we discover, validate, and demonstrate glycotemplating through comparison to established computational results and methods, comparison to published experimental results, and prediction of novel experimental results across pathogenic gene variants, evolution, viral proteins, and antibodies.

Figure 2 **– N- and O-glycan substructures associated with glycosite-proximal protein structure. (a)** Dimensionality reduction trained on UniCarbKB glycosite structures. When projected into the UniCarbKB-trained space, all human Uniprot annotated glycosites in appear within original density implying that UniCarbKB glycosites are sufficiently representative of most documented glycosites. The scatterplots show a two-dimensional projection of the FAMD using a Uniform Manifold Approximation and Projection (UMAP).[37] Each point is a site on a glycoprotein, each color indicates the source of that protein. (**b**) Volcano plot of the log odds ratio and False Discovery Rate adjusted p-values from a Fisher exact test between glycan and protein structure occurrence. We observe many large and significant Intermolecular Relations (IMR), with most significant relations associated with alanine, cysteine, valine, and glutamine (A, C, V, Q, respectively). (**c**) Inter-Molecular Relations (IMR) were also estimated by logistic GEE controlling for protein-bias. The number of significant (FDR<0.1, |log(OR)|>0.1) IMR relating to structurally proximal AAs (N+6Å), sequence proximal AAs C-terminal (N+5), N-terminal (N-5) or either direction (N+/-5), predicted secondary structure from sequence (SSpro8) and structure (DSSP): alpha-helix (ss.H), extended strand (ss.E), beta-bridge (ss.B), turn (ss.T) bend (ss.S), other (ss.C).

Figure 3 **– Glycosite-proximal amino acids impact glycosylation.** Specific Inter-Molecular Relations (IMR) were discovered by logistic GEE controlling for protein-bias. **(a-b)** IMR (FDR<0.1, |log(OR)|>0.1) relating structurally proximal amino acids to motifs stratified by the number of Sialic Acids (**a**) and 4-Sulfated GalNAc (**b**). **(c)** Spearman correlation between the monosaccharide count of glycan substructures from protein-structure features; protein structure features with an average absolute correlation > 0.2 were retained. Terms used here are consistent with panel **a** but "aa" denotes a structurally proximal amino acid, "aaUp," "aaDown," and "aaAll" denotes N-terminus, C-terminus, or any sequence proximal amino acid. (**d-e**) IMR (FDR<0.1, |log(OR)|>0.1) compared across two sequence-proximal (d) and spatially proximal (**e**) amino acids, phenylalanine (F) and tryptophan (W). The direct comparison of proximal-amino acid effects visualized the expected change in glycosylation associated with that substitution. (**f**) Network depicting the glycoimpact (see ***Methods***) of spatially proximal (within 5Å) substitutions for structurally low impact (Blosum64) substitutions. Panel **f** shows glycoimpact predicted from BLAMO 0.5:0.1 (|log(OR)| > 0.5, FDR<0.1), see *Supplementary* ***Figure*** *5* for additional thresholds, raw scores and sequence-proximal substitution predictions. Note that plots including glycan substructures were manually curated to summarize the selected glycan substructures. (**g**) Overview of data flow and concepts examined in this manuscript.

Figure 4 **- Glycoimpact of amino acid substitution correlate with evolution metrics and conservation.** (**a**) Comparison of the error between the PAM and BLOSUM substitution matrices and the glycoimpact for corresponding substitutions. Linear regressions are split into null glycoimpact (<2.5) and glycoimpactful (>2.5). Glycoimpact scores from BLAMO 0.5:0.1 were used; those computed from strong IMR (|log(OR)| > 0.5, FDR<0.1). Error (y-axis) was calculated as the root mean square error between PAM and BLOSUM scores. Correlation (R) significance indicated as <0.001 (***), <0.01 (**), and <0.05 (*). (**b**) Glycosite Alignments [12] corresponding to GlyConnect-documented tetraantennary structures (Hex:7 HexNAc:6) with no sialic acid or fucose. See *Supplementary* ***Figure*** *9* for full alignment. The first (top line) and second (bottom line) most popular amino acids are displayed for each position N+/-30. Consensus AAs consistent with other analyses are highlighted in bold and marked with a "+" (Glycosite-coupled, ***Figure*** *4*h) or "*" (high-influence AA, ***Figure*** *2*c). (**c**) An aggregation of all residue-glycosite enrichments at N+/-10 (hypergeometric enrichment illustrated in panel *Supplementary* ***Figure*** *7*c). The proportion of high-ranking Evolutionary Couplings (EC) for each amino acid (rows) at the column-specified relative position was compared with glycosites (GN), asparagines (N), or any residue (X). An opaque red circle indicates that for the residue (row) in the given position (column), high-EC proportion is higher with GN than N. An opaque black triangle indicates high-EC proportion is higher with GN than X. A transparent circle or square indicates GN was not significantly more coupled (hypergeometric test). Significance was assessed at multiple EC-rank thresholds between L/3 and 3L (see Methods) and pooled using Fisher's method (FDR <0.1). (**d**) Hierarchical clustering of coupling-masked (Rank<4L) amino acids surrounding a glycosite (+/-6 AA). Each of 5 clusters was summarized as a motif. Height is the log of cumulative reciprocal EC-Rank with a pseudo-count of 0.25. The

asparagine at the center was fixed at 2 for context. Residues are colored by chemical properties. A more granular clustering, 25 clusters is included in the supplement (*Supplementary* ***Figure*** *8*).

Figure *5* - **Substitution glycoimpact predicts pathogenicity.** (**a**) Boxplots show the min-distance from all residues within human PrP to the N197 or N181 glycosylation sites. Residues are stratified by all sites (All) and causative mutations of prion disease including Creutzfeldt-Jakob disease (CJD) and Gerstmann-Straussler disease (GSS), (one-sided Wilcoxon test). For glycositesite-specific proximity, see *Supplementary* ***Figure*** *11*. (**b**) A hierarchical clustered heatmap (average-linkage with Euclidean distance) of Spearman correlations coefficients between glycoimpact (BLAMO 0.5:0.1) and error between variant impact prediction scores. Prediction-type and protein structure indicate the training data used to build various tools as described in dbNSFP [40]. Each row and column refer to a variant function prediction tool. (**c**) Null and impactful glycoimpact (BLAMO 0.5:0.1) stratified by variant pathogenicity in ClinVar within 20Å (min-distance) of an N-glycosylation site. Two-dimensional density plots compare glycoimpact and the glycosite-mutation distance.

Figure *6* – Changes in high-mannose, hybrid, and complex glycosylation are predicted by glycosite-proximal high-glycoimpact substitutions in HIV, SARS-CoV2. (**a**) GEE-calculated IMR from PGES-DB denoting relations between sequence (triangle & square) or structural protein features (circle & plus) and motifs containing >3 mannose (hybrid & high-mannose). (**b**) The range of mass spectrometry peaks consistent with either oligomannose or hybrid glycans (N203) or complex glycan peaks (N3) at each site on the HIV envelope gp160 (BG505 SOSIP.664, PDB:4TVP).[66] Relative abundance is represented as a ratio of oligomannose-hybrid to complex glycan peaks (N203/N3). (**c**) Distributions of oligomannose-hybrid to complexity (N203/N3, panel **b**) glycan peaks stratified by proximal protein structure features selected in panel **a**. For the N203/N3 distribution of select IMR, see *Supplementary* ***Figure*** *12*. (**d**) Mean proportion of mass-spectrometry-observed peptide with mass offsets corresponding to complex glycan peaks (+3, purple), oligomannose or hybrid glycan peaks (+203, green), or no glycosylation (+0, grey) in the SARS-CoV-2 S1 subunit at 3 sites with significant glycosylation differences between the original ancestral strain, and the Delta and Gamma variants (see *Supplementary* ***Figure*** *13* for all sites). Peak count for each glycosylation offset type (+3, +203, or +0) for each glycosylation site is divided by the total number of peaks for that site to determine the site-specific proportion of each glycosylation type. Significant differential glycosylation (FDR<0.05) in VOC compared to ancestral is indicated by "*".

Figure *7* –Differential glycosylation is predicted by high-glycoimpact events near glycosylation sites in IgG (**a**) GEE-learned IMR relating to sequence-proximal (upstream/N-terminal) effects of I and F. IgG allotypes, F299 and I299, segregated by Principal Component Analysis of relative abundance (**b**) separate by allotype, not strain. (**c**) Galactose (Gal), Sialylation (Neu5Ac) and Bisecting GlcNAc abundance distributions for IgG1 F299 and I299 allotypes across BALB/c and C57BL/6 mice (see *Supplementary* ***Figure*** *14*). (**d-e**) Core-fucose preference (see **Methods,** *Supplementary* ***Figure*** *15*) for each glycosite-proximal variant in the REFORM Fc variant panel.[74] Variants are colored by index. (**d**) Variants are stratified continuously (top) by percent of fucosylated Fc-cleaved glycans observed on the 24C5 monoclonal antibody. (**e**) Variants are stratified categorically (bottom) by association with enhanced ADCC.[74] Variants appearing in Fc regions associated with both no-enhancement and enhanced ADCC are shown as transparent. Only L235A and G236A are uniquely associated with ADCC.

References

1. Varki, A., Cummings, R.D., Aebi, M., Packer, N.H., Seeberger, P.H., Esko, J.D., Stanley, P., Hart, G., Darvill, A., Kinoshita, T., et al. (2015). Symbol Nomenclature for Graphical Representations of Glycans. Glycobiology *25*, 1323–1324.

2. Neelamegham, S., Aoki-Kinoshita, K., Bolton, E., Frank, M., Lisacek, F., Lütteke, T., O'Boyle, N., Packer, N.H., Stanley, P., Toukach, P., et al. (2019). Updates to the Symbol Nomenclature for Glycans guidelines. Glycobiology *29*, 620–624.

3. Pothukuchi, P., Agliarulo, I., Russo, D., Rizzo, R., Russo, F., and Parashuraman, S. (2019). Translation of genome to glycome: role of the Golgi apparatus. FEBS Lett. *593*, 2390–2411.

4. Johnson, R.L., and Deutsch, H.F. (1970). Preparation and studies of myeloma Fab subfractions. Immunochemistry *7*, 207–215.

5. Marshall, R.D. (1974). The nature and metabolism of the carbohydrate-peptide linkages of glycoproteins. Biochem. Soc. Symp., 17–26.

6. Shakin-Eshleman, S.H., Spitalnik, S.L., and Kasturi, L. (1996). The amino acid at the X position of an Asn-X-Ser sequon is an important determinant of N-linked core-glycosylation efficiency. J. Biol. Chem. *271*, 6363–6366.

7. Petrescu, A.-J., Milac, A.-L., Petrescu, S.M., Dwek, R.A., and Wormald, M.R. (2004). Statistical analysis of the protein environment of N-glycosylation sites: implications for occupancy, structure, and folding. Glycobiology *14*, 103–114.

8. Kasturi, L., Eshleman, J.R., Wunner, W.H., and Shakin-Eshleman, S.H. (1995). The hydroxy amino acid in an Asn-X-Ser/Thr sequon can influence N-linked core glycosylation efficiency and the level of expression of a cell surface glycoprotein. J. Biol. Chem. *270*, 14756–14761.

9. Lund, J., Takahashi, N., Pound, J.D., Goodall, M., and Jefferis, R. (1996). Multiple interactions of IgG with its core oligosaccharide can modulate recognition by complement and human Fc gamma receptor I and influence the synthesis of its oligosaccharide chains. The Journal of Immunology *157*, 4963–4969.

10. Altman, M.O., Angel, M., Košík, I., Trovão, N.S., Zost, S.J., Gibbs, J.S., Casalino, L., Amaro, R.E., Hensley, S.E., Nelson, M.I., et al. (2019). Human Influenza A Virus Hemagglutinin Glycan Evolution Follows a Temporal Pattern to a Glycan Limit. Preprint, 10.1128/mbio.00204-19 10.1128/mbio.00204-19.

11. Yu, W.-H., Zhao, P., Draghi, M., Arevalo, C., Karsten, C.B., Suscovich, T.J., Gunn, B., Streeck, H., Brass, A.L., Tiemeyer, M., et al. (2018). Exploiting glycan topography for computational design of Env glycoprotein antigenicity. PLoS Comput. Biol. *14*, e1006093.

12. Gastaldello, A., Alocci, D., Baeriswyl, J.-L., Mariethoz, J., and Lisacek, F. (2016). GlycoSiteAlign: Glycosite Alignment Based on Glycan Structure. J. Proteome Res. *15*, 3916–3928.

883 13. Huang, Y.-W., Yang, H.-I., Wu, Y.-T., Hsu, T.-L., Lin, T.-W., Kelly, J.W., and Wong, C.-H. (2017).
884 Residues comprising the enhanced aromatic sequon influence protein N-glycosylation efficiency. J.
885 Am. Chem. Soc. *139*, 12947–12955.

886 14. Murray, A.N., Chen, W., Antonopoulos, A., Hanson, S.R., Wiseman, R.L., Dell, A., Haslam, S.M.,
887 Powers, D.L., Powers, E.T., and Kelly, J.W. (2015). Enhanced aromatic sequons increase
888 oligosaccharyltransferase glycosylation efficiency and glycan homogeneity. Chem. Biol. *22*, 1052–
889 1062.

890 15. Gupta, R., and Brunak, S. (2002). Prediction of glycosylation across the human proteome and the
891 correlation to protein function. Pac. Symp. Biocomput., 310–322.

892 16. Steentoft, C., Vakhrushev, S.Y., Joshi, H.J., Kong, Y., Vester-Christensen, M.B., Schjoldager, K.T.-B.G.,
893 Lavrsen, K., Dabelsteen, S., Pedersen, N.B., Marcos-Silva, L., et al. (2013). Precision mapping of the
894 human O-GalNAc glycoproteome through SimpleCell technology. EMBO J. *32*, 1478–1488.

895 17. Ives, C.M., Singh, O., D'Andrea, S., Fogarty, C.A., Harbison, A.M., Satheesan, A., Tropea, B., and
896 Fadda, E. (2023). Restoring Protein Glycosylation with GlycoShape. bioRxiv.
897 10.1101/2023.12.11.571101.

898 18. Blom, N., Sicheritz-Pontén, T., Gupta, R., Gammeltoft, S., and Brunak, S. (2004). Prediction of post-
899 translational glycosylation and phosphorylation of proteins from the amino acid sequence.
900 Proteomics *4*, 1633–1649.

901 19. Silverman, J.M., and Imperiali, B. (2016). Bacterial N-Glycosylation Efficiency Is Dependent on the
902 Structural Context of Target Sequons. J. Biol. Chem. *291*, 22001–22010.

903 20. Kawatkar, S.P., Kuntz, D.A., Woods, R.J., Rose, D.R., and Boons, G.-J. (2006). Structural Basis of the
904 Inhibition of Golgi α-Mannosidase II by Mannostatin A and the Role of the Thiomethyl Moiety in
905 Ligand−Protein Interactions. Preprint, 10.1021/ja061216p 10.1021/ja061216p.

906 21. Li, B., Kawatkar, S.P., George, S., Strachan, H., Woods, R.J., Siriwardena, A., Moremen, K.W., and
907 Boons, G.-J. (2004). Inhibition of Golgi Mannosidase II with Mannostatin A Analogues: Synthesis,
908 Biological Evaluation, and Structure-Activity Relationship Studies. Chembiochem *5*, 1220–1227.

909 22. Hang, I., Lin, C.-W., Grant, O.C., Fleurkens, S., Villiger, T.K., Soos, M., Morbidelli, M., Woods, R.J.,
910 Gauss, R., and Aebi, M. (2015). Analysis of site-specific N-glycan remodeling in the endoplasmic
911 reticulum and the Golgi. Glycobiology *25*, 1335–1349.

912 23. Xiang, Y., Karaveg, K., and Moremen, K.W. (2016). Substrate recognition and catalysis by GH47 α-
913 mannosidases involved in Asn-linked glycan maturation in the mammalian secretory pathway. Proc.
914 Natl. Acad. Sci. U. S. A. *113*, E7890–E7899.

915 24. Thaysen-Andersen, M., and Packer, N.H. (2012). Site-specific glycoproteomics confirms that protein
916 structure dictates formation of N-glycan type, core fucosylation and branching. Glycobiology *22*,
917 1440–1452.

918 25. Allen, J.D., Chawla, H., Samsudin, F., Zuzic, L., Shivgan, A.T., Watanabe, Y., He, W.-T., Callaghan, S.,
919 Song, G., Yong, P., et al. (2021). Site-specific steric control of SARS-CoV-2 spike glycosylation. Cold
920 Spring Harbor Laboratory, 2021.03.08.433764. 10.1101/2021.03.08.433764.

921 26. García-García, A., Serna, S., Yang, Z., Delso, I., Taleb, V., Hicks, T., Artschwager, R., Vakhrushev, S.Y.,
922 Clausen, H., Angulo, J., et al. (2021). FUT8-directed core fucosylation of N-glycans is regulated by
923 the glycan structure and protein environment. ACS Catal. *11*, 9052–9065.

924 27. Losfeld, M.-E., Scibona, E., Lin, C.-W., Villiger, T.K., Gauss, R., Morbidelli, M., and Aebi, M. (2017).
925 Influence of protein/glycan interaction on site-specific glycan heterogeneity. FASEB J. *31*, 4623–
926 4635.

927 28. Losfeld, M.-E., Scibona, E., Lin, C.-W., and Aebi, M. (2022). Glycosylation network mapping and site-
928 specific glycan maturation in vivo. iScience, 105417.

929 29. Mathew, C., Weiß, R.G., Giese, C., Lin, C.-W., Losfeld, M.-E., Glockshuber, R., Riniker, S., and Aebi,
930 M. (2021). Glycan-protein interactions determine kinetics of N-glycan remodeling. RSC Chem Biol *2*,
931 917–931.

932 30. Adams, T.M., Zhao, P., Chapla, D., Moremen, K.W., and Wells, L. (2022). Sequential in vitro
933 enzymatic N-glycoprotein modification reveals site-specific rates of glycoenzyme processing. J. Biol.
934 Chem., 102474.

935 31. Bagdonas, H., Fogarty, C.A., Fadda, E., and Agirre, J. (2021). The case for post-predictional
936 modifications in the AlphaFold Protein Structure Database. Nat. Struct. Mol. Biol. *28*, 869–870.

937 32. Tsai, Y.-X., Chang, N.-E., Reuter, K., Chang, H.-T., Yang, T.-J., von Bülow, S., Sehrawat, V., Zerrouki,
938 N., Tuffery, M., Gecht, M., et al. (2024). Rapid simulation of glycoprotein structures by grafting and
939 steric exclusion of glycan conformer libraries. Cell *187*, 1296-1311.e26.

940 33. Abramson, J., Adler, J., Dunger, J., Evans, R., Green, T., Pritzel, A., Ronneberger, O., Willmore, L.,
941 Ballard, A.J., Bambrick, J., et al. (2024). Accurate structure prediction of biomolecular interactions
942 with AlphaFold 3. Nature. 10.1038/s41586-024-07487-w.

943 34. Alocci, D., Mariethoz, J., Gastaldello, A., Gasteiger, E., Karlsson, N.G., Kolarich, D., Packer, N.H., and
944 Lisacek, F. (2019). GlyConnect: Glycoproteomics Goes Visual, Interactive, and Analytical. J.
945 Proteome Res. *18*, 664–677.

946 35. Bao, B., Kellman, B.P., Chiang, A.W.T., Zhang, Y., Sorrentino, J.T., York, A.K., Mohammad, M.A.,
947 Haymond, M.W., Bode, L., and Lewis, N.E. (2021). Correcting for sparsity and interdependence in
948 glycomics by accounting for glycan biosynthesis. Nat. Commun. *12*, 4988.

949 36. Mih, N., Brunk, E., Chen, K., Catoiu, E., Sastry, A., Kavvas, E., Monk, J.M., Zhang, Z., and Palsson, B.O.
950 (2018). ssbio: a Python framework for structural systems biology. Bioinformatics *34*, 2155–2157.

951 37. McInnes, L., Healy, J., and Melville, J. (2018). UMAP: Uniform Manifold Approximation and
952 Projection for Dimension Reduction. arXiv [stat.ML].

953 38. Campbell, M.P., Peterson, R., Mariethoz, J., Gasteiger, E., Akune, Y., Aoki-Kinoshita, K.F., Lisacek, F.,
954 and Packer, N.H. (2014). UniCarbKB: building a knowledge platform for glycoproteomics. Nucleic
955 Acids Res. *42*, D215-21.

956 39. Uhlén, M., Fagerberg, L., Hallström, B.M., Lindskog, C., Oksvold, P., Mardinoglu, A., Sivertsson, Å.,
957 Kampf, C., Sjöstedt, E., Asplund, A., et al. (2015). Proteomics. Tissue-based map of the human

958 proteome. Science *347*, 1260419.

959 40. Liu, X., Wu, C., Li, C., and Boerwinkle, E. (2016). DbNSFP v3.0: A one-stop database of functional
960 predictions and annotations for human nonsynonymous and splice-site SNVs. Hum. Mutat. *37*,
961 235–241.

962 41. Fitch, W.M., and Dayhoff, M.O. (1973). Atlas of protein sequence and structure, 1972. Syst. Zool.
963 *22*, 196.

964 42. Henikoff, S., and Henikoff, J.G. (1992). Amino acid substitution matrices from protein blocks. Proc.
965 Natl. Acad. Sci. U. S. A. *89*, 10915–10919.

966 43. Mount, D.W. (2008). Comparison of the PAM and BLOSUM amino acid substitution matrices. CSH
967 Protoc. *2008*, db.ip59.

968 44. Pearson, W.R. (2013). Selecting the right similarity-scoring matrix. Curr. Protoc. Bioinformatics *43*,
969 3.5.1-3.5.9.

970 45. Marks, D.S., Colwell, L.J., Sheridan, R., Hopf, T.A., Pagnani, A., Zecchina, R., and Sander, C. (2011).
971 Protein 3D structure computed from evolutionary sequence variation. PLoS One *6*, e28766.

972 46. Thusberg, J., Olatubosun, A., and Vihinen, M. (2011). Performance of mutation pathogenicity
973 prediction methods on missense variants. Hum. Mutat. *32*, 358–368.

974 47. Cheng, N., Li, M., Zhao, L., Zhang, B., Yang, Y., Zheng, C.-H., and Xia, J. (2020). Comparison and
975 integration of computational methods for deleterious synonymous mutation prediction. Brief.
976 Bioinform. *21*, 970–981.

977 48. Simeonov, D.R., Wang, X., Wang, C., Sergeev, Y., Dolinska, M., Bower, M., Fischer, R., Winer, D.,
978 Dubrovsky, G., Balog, J.Z., et al. (2013). DNA variations in oculocutaneous albinism: an updated
979 mutation list and current outstanding issues in molecular diagnostics. Hum. Mutat. *34*, 827–835.

980 49. Spritz, R.A., Ho, L., Furumura, M., and Hearing, V.J., Jr (1997). Mutational analysis of copper binding
981 by human tyrosinase. J. Invest. Dermatol. *109*, 207–212.

982 50. Halaban, R., Svedine, S., Cheng, E., Smicun, Y., Aron, R., and Hebert, D.N. (2000). Endoplasmic
983 reticulum retention is a common defect associated with tyrosinase-negative albinism. Proc. Natl.
984 Acad. Sci. U. S. A. *97*, 5889–5894.

985 51. Branza-Nichita, N., Negroiu, G., Petrescu, A.J., Garman, E.F., Platt, F.M., Wormald, M.R., Dwek, R.A.,
986 and Petrescu, S.M. (2000). Mutations at critical N-glycosylation sites reduce tyrosinase activity by
987 altering folding and quality control. J. Biol. Chem. *275*, 8169–8175.

988 52. Dolinska, M.B., Kovaleva, E., Backlund, P., Wingfield, P.T., Brooks, B.P., and Sergeev, Y.V. (2014).
989 Albinism-causing mutations in recombinant human tyrosinase alter intrinsic enzymatic activity.
990 PLoS One *9*, e84494.

991 53. Dolinska, M.B., and Sergeev, Y.V. (2017). The consequences of deglycosylation of recombinant
992 intra-melanosomal domain of human tyrosinase. Biol. Chem. *399*, 73–77.

993 54. Sevillano, A.M., Aguilar-Calvo, P., Kurt, T.D., Lawrence, J.A., Soldau, K., Nam, T.H., Schumann, T.,
994 Pizzo, D.P., Nyström, S., Choudhury, B., et al. (2020). Prion protein glycans reduce intracerebral
995 fibril formation and spongiosis in prion disease. J. Clin. Invest. *130*, 1350–1362.

996 55. Yi, C.-W., Wang, L.-Q., Huang, J.-J., Pan, K., Chen, J., and Liang, Y. (2018). Glycosylation Significantly
997 Inhibits the Aggregation of Human Prion Protein and Decreases Its Cytotoxicity. Preprint,
998 10.1038/s41598-018-30770-6 10.1038/s41598-018-30770-6.

999 56. Ng, B.G., and Freeze, H.H. (2018). Perspectives on Glycosylation and Its Congenital Disorders.
1000 Trends Genet. *34*, 466–476.

1001 57. Joshi, H.J., Hansen, L., Narimatsu, Y., Freeze, H.H., Henrissat, B., Bennett, E., Wandall, H.H., Clausen,
1002 H., and Schjoldager, K.T. (2018). Glycosyltransferase genes that cause monogenic congenital
1003 disorders of glycosylation are distinct from glycosyltransferase genes associated with complex
1004 diseases. Glycobiology *28*, 284–294.

1005 58. Berg-Fussman, A., Grace, M.E., Ioannou, Y., and Grabowski, G.A. (1993). Human acid beta-
1006 glucosidase. N-glycosylation site occupancy and the effect of glycosylation on enzymatic activity. J.
1007 Biol. Chem. *268*, 14861–14866.

1008 59. Pol-Fachin, L., Siebert, M., Verli, H., and Saraiva-Pereira, M.L. (2016). Glycosylation is crucial for a
1009 proper catalytic site organization in human glucocerebrosidase. Glycoconj. J. *33*, 237–244.

1010 60. Smith, L., Mullin, S., and Schapira, A.H.V. (2017). Insights into the structural biology of Gaucher
1011 disease. Exp. Neurol. *298*, 180–190.

1012 61. Souffrant, M.G., Yao, X.-Q., Momin, M., and Hamelberg, D. (2020). N-glycosylation and gaucher
1013 disease mutation allosterically alter active-site dynamics of acid-β-glucosidase. ACS Catal. *10*, 1810–
1014 1820.

1015 62. Di Fede, G., Catania, M., Atzori, C., Moda, F., Pasquali, C., Indaco, A., Grisoli, M., Zuffi, M., Guaita,
1016 M.C., Testi, R., et al. (2019). Clinical and neuropathological phenotype associated with the novel
1017 V189I mutation in the prion protein gene. Acta Neuropathol. Commun. *7*, 1.

1018 63. Ladogana, A., and Kovacs, G.G. (2018). Genetic Creutzfeldt–Jakob disease. In Human Prion Diseases
1019 Handbook of clinical neurology. (Elsevier), pp. 219–242.

1020 64. Liberski, P.P. (2012). Gerstmann-Sträussler-Scheinker disease. Adv. Exp. Med. Biol. *724*, 128–137.

1021 65. Cohen, M.L. (2014). Human Prion Diseases. In Pathobiology of Human Disease (Elsevier), pp. 2045–
1022 2054.

1023 66. Cao, L., Diedrich, J.K., Kulp, D.W., Pauthner, M., He, L., Park, S.-K.R., Sok, D., Su, C.Y., Delahunty,
1024 C.M., Menis, S., et al. (2017). Global site-specific N-glycosylation analysis of HIV envelope
1025 glycoprotein. Preprint, 10.1038/ncomms14954 10.1038/ncomms14954.

1026 67. Zhao, P., Praissman, J.L., Grant, O.C., Cai, Y., Xiao, T., Rosenbalm, K.E., Aoki, K., Kellman, B.P.,
1027 Bridger, R., Barouch, D.H., et al. (2020). Virus-Receptor Interactions of Glycosylated SARS-CoV-2
1028 Spike and Human ACE2 Receptor. Cell Host Microbe *28*, 586-601.e6.

1029 68. Watanabe, Y., Allen, J.D., Wrapp, D., McLellan, J.S., and Crispin, M. (2020). Site-specific glycan
1030 analysis of the SARS-CoV-2 spike. Science *369*, 330–333.

1031 69. Casalino, L., Gaieb, Z., Dommer, A.C., and Harbison, A.M. (2020). Shielding and Beyond: The Roles
1032 of Glycans in SARS-CoV-2 Spike Protein. bioRxiv.

1033 70. Grant, O.C., Montgomery, D., Ito, K., and Woods, R.J. (2020). 3D Models of glycosylated SARS-CoV-2
1034 spike protein suggest challenges and opportunities for vaccine development. bioRxiv.

1035 71. Wintjens, R., Bifani, A.M., and Bifani, P. (2020). Impact of glycan cloud on the B-cell epitope
1036 prediction of SARS-CoV-2 Spike protein. NPJ Vaccines *5*, 81.

1037 72. Zhang, L., Mann, M., Syed, Z.A., Reynolds, H.M., Tian, E., Samara, N.L., Zeldin, D.C., Tabak, L.A., and
1038 Ten Hagen, K.G. (2021). Furin cleavage of the SARS-CoV-2 spike is modulated by O-glycosylation.
1039 Proc. Natl. Acad. Sci. U. S. A. *118*, e2109905118.

1040 73. Baboo, S., Diedrich, J.K., Martínez-Bartolomé, S., Wang, X., Schiffner, T., Groschel, B., Schief, W.R.,
1041 Paulson, J.C., and Yates, J.R., 3rd (2021). DeGlyPHER: An ultrasensitive method for the analysis of
1042 viral spike N-glycoforms. Anal. Chem. *93*, 13651–13657.

1043 74. Gunn, B.M., Lu, R., Slein, M.D., Ilinykh, P.A., Huang, K., Atyeo, C., Schendel, S.L., Kim, J., Cain, C.,
1044 Roy, V., et al. (2021). A Fc engineering approach to define functional humoral correlates of
1045 immunity against Ebola virus. Immunity *54*, 815-828.e5.

1046 75. Krištić, J., Zaytseva, O.O., Ram, R., Nguyen, Q., Novokmet, M., Vučković, F., Vilaj, M., Trbojević-
1047 Akmačić, I., Pezer, M., Davern, K.M., et al. (2018). Profiling and genetic control of the murine
1048 immunoglobulin G glycome. Nat. Chem. Biol. *14*, 516–524.

1049 76. Cheng, H.D., Tirosh, I., de Haan, N., Stöckmann, H., Adamczyk, B., McManus, C.A., O'Flaherty, R.,
1050 Greville, G., Saldova, R., Bonilla, F.A., et al. (2020). IgG Fc glycosylation as an axis of humoral
1051 immunity in childhood. J. Allergy Clin. Immunol. *145*, 710-713.e9.

1052 77. Lofano, G., Gorman, M.J., Yousif, A.S., Yu, W.-H., Fox, J.M., Dugast, A.-S., Ackerman, M.E.,
1053 Suscovich, T.J., Weiner, J., Barouch, D., et al. (2018). Antigen-specific antibody Fc glycosylation
1054 enhances humoral immunity via the recruitment of complement. Sci. Immunol. *3*, eaat7796.

1055 78. Atyeo, C., Pullen, K.M., Bordt, E.A., Fischinger, S., Burke, J., Michell, A., Slein, M.D., Loos, C., Shook,
1056 L.L., Boatin, A.A., et al. (2021). Compromised SARS-CoV-2-specific placental antibody transfer. Cell
1057 *184*, 628-642.e10.

1058 79. Grace, P.S., Dolatshahi, S., Lu, L.L., Cain, A., Palmieri, F., Petrone, L., Fortune, S.M., Ottenhoff,
1059 T.H.M., Lauffenburger, D.A., Goletti, D., et al. (2021). Antibody subclass and glycosylation shift
1060 following effective TB treatment. Front. Immunol. *12*, 679973.

1061 80. Majewska, N.I., Tejada, M.L., Betenbaugh, M.J., and Agarwal, N. (2020). N-glycosylation of IgG and
1062 IgG-like recombinant therapeutic proteins: Why is it important and how can we control it? Annu.
1063 Rev. Chem. Biomol. Eng. *11*, 311–338.

1064 81. Li, W., Zhu, Z., Chen, W., Feng, Y., and Dimitrov, D.S. (2017). Crystallizable fragment
1065 glycoengineering for therapeutic antibodies development. Front. Immunol. *8*.

1066 10.3389/fimmu.2017.01554.

1067 82. Zhang, P., Woen, S., Wang, T., Liau, B., Zhao, S., Chen, C., Yang, Y., Song, Z., Wormald, M.R., Yu, C.,
1068 et al. (2016). Challenges of glycosylation analysis and control: an integrated approach to producing
1069 optimal and consistent therapeutic drugs. Drug Discov. Today *21*, 740–765.

1070 83. Shields, R.L., Lai, J., Keck, R., O'Connell, L.Y., Hong, K., Meng, Y.G., Weikert, S.H.A., and Presta, L.G.
1071 (2002). Lack of Fucose on Human IgG1 N-Linked Oligosaccharide Improves Binding to Human FcγRIII
1072 and Antibody-dependent Cellular Toxicity. J. Biol. Chem. *277*, 26733–26740.

1073 84. de Haan, N., Reiding, K.R., Krištić, J., Hipgrave Ederveen, A.L., Lauc, G., and Wuhrer, M. (2017). The
1074 N-Glycosylation of Mouse Immunoglobulin G (IgG)-Fragment Crystallizable Differs Between IgG
1075 Subclasses and Strains. Front. Immunol. *8*, 608.

1076 85. Zaytseva, O.O., Jansen, B.C., Hanić, M., Mrčela, M., Razdorov, G., Stojković, R., Erhardt, J., Brizić, I.,
1077 Jonjić, S., Pezer, M., et al. (2018). MIgGGly (mouse IgG glycosylation analysis) - a high-throughput
1078 method for studying Fc-linked IgG N-glycosylation in mice with nanoUPLC-ESI-MS. Sci. Rep. *8*,
1079 13688.

1080 86. Zaytseva, O.O., Seeling, M., Krištić, J., Lauc, G., Pezer, M., and Nimmerjahn, F. (2020). Fc-Linked IgG
1081 N-Glycosylation in FcγR Knock-Out Mice. Preprint, 10.3389/fcell.2020.00067
1082 10.3389/fcell.2020.00067.

1083 87. Karch, C.P., Paquin-Proulx, D., Eller, M.A., Matyas, G.R., Burkhard, P., and Beck, Z. (2020). Impact of
1084 the expression system on the immune responses to self-assembling protein nanoparticles (SAPNs)
1085 displaying HIV-1 V1V2 loop. Nanomedicine *29*, 102255.

1086 88. Hombu, R., Neelamegham, S., and Park, S. (2021). Cellular and molecular engineering of glycan
1087 sialylation in heterologous systems. Molecules *26*, 5950.

1088 89. Zhong, X., Ma, W., Meade, C.L., Tam, A.S., Llewellyn, E., Cornell, R., Cote, K., Scarcelli, J.J., Marshall,
1089 J.K., Tzvetkova, B., et al. (2019). Transient CHO expression platform for robust antibody production
1090 and its enhanced N-glycan sialylation on therapeutic glycoproteins. Biotechnol. Prog. *35*, e2724.

1091 90. Zhong, X., Schwab, A., Ma, W., Meade, C.L., Zhou, J., D'Antona, A.M., Somers, W., and Lin, L. (2022).
1092 Large-scale transient production in ExpiCHO-S^{TM} with enhanced N-galactosylation-sialylation and
1093 PEI-based transfection. Methods Mol. Biol. *2313*, 143–150.

1094 91. Hudson, K.L., Bartlett, G.J., Diehl, R.C., Agirre, J., Gallagher, T., Kiessling, L.L., and Woolfson, D.N.
1095 (2015). Carbohydrate-aromatic interactions in proteins. J. Am. Chem. Soc. *137*, 15152–15160.

1096 92. Chen, W., Enck, S., Price, J.L., Powers, D.L., Powers, E.T., Wong, C.-H., Dyson, H.J., and Kelly, J.W.
1097 (2013). Structural and energetic basis of carbohydrate-aromatic packing interactions in proteins. J.
1098 Am. Chem. Soc. *135*, 9877–9884.

1099 93. Asensio, J.L., Ardá, A., Cañada, F.J., and Jiménez-Barbero, J. (2013). Carbohydrate-aromatic
1100 interactions. Acc. Chem. Res. *46*, 946–954.

1101 94. Montalvillo-Jiménez, L., Santana, A.G., Corzana, F., Jiménez-Osés, G., Jiménez-Barbero, J., Gómez,
1102 A.M., and Asensio, J.L. (2019). Impact of aromatic stacking on glycoside reactivity: Balancing CH/π

1103 and cation/π interactions for the stabilization of glycosyl-oxocarbenium ions. J. Am. Chem. Soc. *141*,
1104 13372–13384.

1105 95. Ardejani, M.S., Noodleman, L., Powers, E.T., and Kelly, J.W. (2021). Stereoelectronic effects in
1106 stabilizing protein-N-glycan interactions revealed by experiment and machine learning. Nat. Chem.
1107 *13*, 480–487.

1108 96. Goldfarb, L.G., Petersen, R.B., Tabaton, M., Brown, P., LeBlanc, A.C., Montagna, P., Cortelli, P.,
1109 Julien, J., Vital, C., and Pendelbury, W.W. (1992). Fatal familial insomnia and familial Creutzfeldt-
1110 Jakob disease: disease phenotype determined by a DNA polymorphism. Science *258*, 806–808.

1111 97. Wang, W.K., Essex, M., and Lee, T.H. (1996). Single amino acid substitution in constant region 1 or 4
1112 of gp120 causes the phenotype of a human immunodeficiency virus type 1 variant with mutations
1113 in hypervariable regions 1 and 2 to revert. J. Virol. *70*, 607–611.

1114 98. Branza-Nichita, N., Petrescu, A.J., Negroiu, G., Dwek, R.A., and Petrescu, S.M. (2000). N-
1115 glycosylation processing and glycoprotein folding-lessons from the tyrosinase-related proteins.
1116 Chem. Rev. *100*, 4697–4712.

1117 99. Dolinska, M.B., Kus, N.J., Farney, S.K., Wingfield, P.T., Brooks, B.P., and Sergeev, Y.V. (2017).
1118 Oculocutaneous albinism type 1: link between mutations, tyrosinase conformational stability, and
1119 enzymatic activity. Pigment Cell Melanoma Res. *30*, 41–52.

1120 100. Grant, O.C., Montgomery, D., Ito, K., and Woods, R.J. (2020). Analysis of the SARS-CoV-2 spike
1121 protein glycan shield reveals implications for immune recognition. Sci. Rep. *10*, 14991.

1122 101. Peng, W., Rayaprolu, V., Parvate, A.D., Pronker, M.F., Hui, S., Parekh, D., Shaffer, K., Yu, X., Saphire,
1123 E.O., and Snijder, J. (2022). Glycan shield of the ebolavirus envelope glycoprotein GP. Commun.
1124 Biol. *5*, 785.

1125 102. Wei, C.-J., Boyington, J.C., Dai, K., Houser, K.V., Pearce, M.B., Kong, W.-P., Yang, Z.-Y., Tumpey,
1126 T.M., and Nabel, G.J. (2010). Cross-neutralization of 1918 and 2009 influenza viruses: role of
1127 glycans in viral evolution and vaccine design. Sci. Transl. Med. *2*, 24ra21.

1128 103. Schulz, M.A., Tian, W., Mao, Y., Van Coillie, J., Sun, L., Larsen, J.S., Chen, Y.-H., Kristensen, C.,
1129 Vakhrushev, S.Y., Clausen, H., et al. (2018). Glycoengineering design options for IgG1 in CHO cells
1130 using precise gene editing. Glycobiology *28*, 542–549.

1131 104. Narimatsu, Y., Joshi, H.J., Nason, R., Van Coillie, J., Karlsson, R., Sun, L., Ye, Z., Chen, Y.-H.,
1132 Schjoldager, K.T., Steentoft, C., et al. (2019). An atlas of human glycosylation pathways enables
1133 display of the human glycome by gene engineered cells. Mol. Cell *75*, 394-407.e5.

1134 105. Narimatsu, Y., Büll, C., Chen, Y.-H., Wandall, H.H., Yang, Z., and Clausen, H. (2021). Genetic
1135 glycoengineering in mammalian cells. J. Biol. Chem. *296*, 100448.

1136 106. Sumit, M., Dolatshahi, S., Chu, A.-H.A., Cote, K., Scarcelli, J.J., Marshall, J.K., Cornell, R.J., Weiss, R.,
1137 Lauffenburger, D.A., Mulukutla, B.C., et al. (2019). Dissecting N-Glycosylation Dynamics in Chinese
1138 Hamster Ovary Cells Fed-batch Cultures using Time Course Omics Analyses. iScience *12*, 102–120.

1139 107. Ehret, J., Zimmermann, M., Eichhorn, T., and Zimmer, A. (2019). Impact of cell culture media

1140 additives on IgG glycosylation produced in Chinese hamster ovary cells. Biotechnol. Bioeng. *116*,
1141 816–830.

1142 108. Fan, Y., Kildegaard, H.F., and Andersen, M.R. (2017). Engineer medium and feed for modulating N-
1143 glycosylation of recombinant protein production in CHO cell culture. Methods Mol. Biol. *1603*, 209–
1144 226.

1145 109. Kotidis, P., and Kontoravdi, C. (2020). Harnessing the potential of artificial neural networks for
1146 predicting protein glycosylation. Metabolic Engineering Communications, e00131.

1147 110. Jimenez del Val, I., Nagy, J.M., and Kontoravdi, C. (2011). A dynamic mathematical model for
1148 monoclonal antibody N-linked glycosylation and nucleotide sugar donor transport within a
1149 maturing Golgi apparatus. Biotechnol. Prog. *27*, 1730–1743.

1150 111. Sou, S.N., Jedrzejewski, P.M., Lee, K., Sellick, C., Polizzi, K.M., and Kontoravdi, C. (2017). Model-
1151 based investigation of intracellular processes determining antibody Fc-glycosylation under mild
1152 hypothermia. Biotechnol. Bioeng. *114*, 1570–1582.

1153 112. Spahn, P.N., Hansen, A.H., Hansen, H.G., Arnsdorf, J., Kildegaard, H.F., and Lewis, N.E. (2016). A
1154 Markov chain model for N-linked protein glycosylation – towards a low-parameter tool for model-
1155 driven glycoengineering. Preprint, 10.1016/j.ymben.2015.10.007 10.1016/j.ymben.2015.10.007.

1156 113. Spahn, P.N., Hansen, A.H., Kol, S., Voldborg, B.G., and Lewis, N.E. (2017). Predictive
1157 glycoengineering of biosimilars using a Markov chain glycosylation model. Biotechnol. J. *12*.
1158 10.1002/biot.201600489.

1159 114. Liang, C., Chiang, A.W.T., Hansen, A.H., Arnsdorf, J., Schoffelen, S., Sorrentino, J.T., Kellman, B.P.,
1160 Bao, B., Voldborg, B.G., and Lewis, N.E. (2020). A Markov model of glycosylation elucidates isozyme
1161 specificity and glycosyltransferase interactions for glycoengineering. Curr Res Biotechnol *2*, 22–36.

1162 115. Michaeli, Y., and Reiter, Y. (2006). Optimised Fc variants with enhanced effector function. Expert
1163 Opin. Ther. Pat. *16*, 1449–1452.

1164 116. Liu, R., Oldham, R.J., Teal, E., Beers, S.A., and Cragg, M.S. (2020). Fc-engineering for modulated
1165 effector functions-improving antibodies for cancer treatment. Antibodies (Basel) *9*, 64.

1166 117. van Erp, E.A., Luytjes, W., Ferwerda, G., and van Kasteren, P.B. (2019). Fc-mediated antibody
1167 effector functions during respiratory syncytial virus infection and disease. Front. Immunol. *10*, 548.

1168 118. Leon, P.E., He, W., Mullarkey, C.E., Bailey, M.J., Miller, M.S., Krammer, F., Palese, P., and Tan, G.S.
1169 (2016). Optimal activation of Fc-mediated effector functions by influenza virus hemagglutinin
1170 antibodies requires two points of contact. Proc. Natl. Acad. Sci. U. S. A. *113*, E5944–E5951.

1171 119. Zhou, M., Palanca, A.M.S., and Law, J.A. (2018). Locus-specific control of the de novo DNA
1172 methylation pathway in Arabidopsis by the CLASSY family. Nat. Genet. *50*, 865–873.

1173 120. Nováček, V., McGauran, G., Matallanas, D., Vallejo Blanco, A., Conca, P., Muñoz, E., Costabello, L.,
1174 Kanakaraj, K., Nawaz, Z., Walsh, B., et al. (2020). Accurate prediction of kinase-substrate networks
1175 using knowledge graphs. PLoS Comput. Biol. *16*, e1007578.

1176 121. Malaker, S.A., Riley, N.M., Shon, D.J., Pedram, K., Krishnan, V., Dorigo, O., and Bertozzi, C.R. (2022).
1177 Revealing the human mucinome. Nat. Commun. *13*, 3542.

1178 122. Madhani, H.D., and Guthrie, C. (1994). Dynamic RNA-RNA interactions in the spliceosome. Annu.
1179 Rev. Genet. *28*, 1–26.

1180 123. Bao, P., Boon, K.-L., Will, C.L., Hartmuth, K., and Lührmann, R. (2018). Multiple RNA–RNA tertiary
1181 interactions are dispensable for formation of a functional U2/U6 RNA catalytic core in the
1182 spliceosome. Preprint, 10.1093/nar/gky966 10.1093/nar/gky966.

1183 124. Corley, M., Burns, M.C., and Yeo, G.W. (2020). How RNA-Binding Proteins Interact with RNA:
1184 Molecules and Mechanisms. Mol. Cell *78*, 9–29.

1185 125. Farnham, P.J., and Platt, T. (1982). Effects of DNA base analogs on transcription termination at the
1186 tryptophan operon attenuator of EScherichia coli. Proc. Natl. Acad. Sci. U. S. A. *79*, 998–1002.

1187 126. Lee, F., and Yanofsky, C. (1977). Transcription termination at the trp operon attenuators of
1188 Escherichia coli and Salmonella typhimurium: RNA secondary structure and regulation of
1189 termination. Proc. Natl. Acad. Sci. U. S. A. *74*, 4365–4369.

1190 127. Oxender, D.L., Zurawski, G., and Yanofsky, C. (1979). Attenuation in the Escherichia coli tryptophan
1191 operon: role of RNA secondary structure involving the tryptophan codon region. Proc. Natl. Acad.
1192 Sci. U. S. A. *76*, 5524–5528.

1193 128. Farnham, P.J., and Platt, T. (1980). A model for transcription termination suggested by studies on
1194 the trp attenuator in vitro using base analogs. Cell *20*, 739–748.

1195 129. Wu, A.M., and Platt, T. (1978). Transcription termination: nucleotide sequence at 3' end of
1196 tryptophan operon in Escherichia coli. Proc. Natl. Acad. Sci. U. S. A. *75*, 5442–5446.

1197 130. Mariethoz, J., Alocci, D., Gastaldello, A., Horlacher, O., Gasteiger, E., Rojas-Macias, M., Karlsson,
1198 N.G., Packer, N.H., and Lisacek, F. (2018). Glycomics@ExPASy: Bridging the Gap. Preprint,
1199 10.1074/mcp.ra118.000799 10.1074/mcp.ra118.000799.

1200 131. York, W.S., Mazumder, R., Ranzinger, R., Edwards, N., Kahsay, R., Aoki-Kinoshita, K.F., Campbell,
1201 M.P., Cummings, R.D., Feizi, T., Martin, M., et al. (2020). GlyGen: Computational and Informatics
1202 Resources for Glycoscience. Glycobiology *30*, 72–73.

1203 132. Cooper, C.A., Joshi, H.J., Harrison, M.J., Wilkins, M.R., and Packer, N.H. (2003). GlycoSuiteDB: a
1204 curated relational database of glycoprotein glycan structures and their biological sources. 2003
1205 update. Nucleic Acids Res. *31*, 511–513.

1206 133. Al Jadda, K., Porterfield, M.P., Bridger, R., Heiss, C., Tiemeyer, M., Wells, L., Miller, J.A., York, W.S.,
1207 and Ranzinger, R. (2015). EUROCarbDB(CCRC): a EUROCarbDB node for storing glycomics standard
1208 data. Bioinformatics *31*, 242–245.

1209 134. Berman, H.M., Westbrook, J., Feng, Z., Gilliland, G., Bhat, T.N., Weissig, H., Shindyalov, I.N., and
1210 Bourne, P.E. (2000). The Protein Data Bank. Nucleic Acids Res. *28*, 235–242.

1211 135. Waterhouse, A., Bertoni, M., Bienert, S., Studer, G., Tauriello, G., Gumienny, R., Heer, F.T., de Beer,

1212 T.A.P., Rempfer, C., Bordoli, L., et al. (2018). SWISS-MODEL: homology modelling of protein
1213 structures and complexes. Nucleic Acids Res. *46*, W296–W303.

1214 136. Yang, J., Yan, R., Roy, A., Xu, D., Poisson, J., and Zhang, Y. (2015). The I-TASSER Suite: protein
1215 structure and function prediction. Nat. Methods *12*, 7–8.

1216 137. Madeira, F., Park, Y.M., Lee, J., Buso, N., Gur, T., Madhusoodanan, N., Basutkar, P., Tivey, A.R.N.,
1217 Potter, S.C., Finn, R.D., et al. (2019). The EMBL-EBI search and sequence analysis tools APIs in 2019.
1218 Nucleic Acids Res. *47*, W636–W641.

1219 138. Zhang, Y., and Sagui, C. (2015). Secondary structure assignment for conformationally irregular
1220 peptides: comparison between DSSP, STRIDE and KAKSI. J. Mol. Graph. Model. *55*, 72–84.

1221 139. Magnan, C.N., and Baldi, P. (2014). SSpro/ACCpro 5: almost perfect prediction of protein secondary
1222 structure and relative solvent accessibility using profiles, machine learning and structural similarity.
1223 Bioinformatics *30*, 2592–2597.

1224 140. Klein, J., and Zaia, J. (2019). glypy: An Open Source Glycoinformatics Library. J. Proteome Res. *18*,
1225 3532–3537.

1226 141. Velankar, S., Dana, J.M., Jacobsen, J., van Ginkel, G., Gane, P.J., Luo, J., Oldfield, T.J., O'Donovan, C.,
1227 Martin, M.-J., and Kleywegt, G.J. (2013). SIFTS: Structure Integration with Function, Taxonomy and
1228 Sequences resource. Nucleic Acids Res. *41*, D483-9.

1229 142. Zeger, S.L., and Liang, K.-Y. (1986). Longitudinal Data Analysis for Discrete and Continuous
1230 Outcomes. Preprint, 10.2307/2531248 10.2307/2531248.

1231 143. Benaglia, T., Chauveau, D., Hunter, D.R., and Young, D. (2009). mixtools: AnRPackage for Analyzing
1232 Finite Mixture Models. Preprint, 10.18637/jss.v032.i06 10.18637/jss.v032.i06.

1233 144. Balakrishnan, S., Kamisetty, H., Carbonell, J.G., Lee, S.-I., and Langmead, C.J. (2011). Learning
1234 generative models for protein fold families. Proteins *79*, 1061–1078.

1235 145. Ekeberg, M., Lövkvist, C., Lan, Y., Weigt, M., and Aurell, E. (2013). Improved contact prediction in
1236 proteins: using pseudolikelihoods to infer Potts models. Phys. Rev. E Stat. Nonlin. Soft Matter Phys.
1237 *87*, 012707.

1238 146. Weinreb, C., Riesselman, A.J., Ingraham, J.B., Gross, T., Sander, C., and Marks, D.S. (2016). 3D RNA
1239 and Functional Interactions from Evolutionary Couplings. Cell *165*, 963–975.

1240 147. Hopf, T.A., Green, A.G., Schubert, B., Mersmann, S., Schärfe, C.P.I., Ingraham, J.B., Toth-Petroczy,
1241 A., Brock, K., Riesselman, A.J., Palmedo, P., et al. (2019). The EVcouplings Python framework for
1242 coevolutionary sequence analysis. Bioinformatics *35*, 1582–1584.

1243 148. Wright, E.S. (2016). Using DECIPHER v2. 0 to analyze big biological sequence data in R. R J. *8*.

1244 149. Wagih, O. (2017). ggseqlogo: a versatile R package for drawing sequence logos. Bioinformatics *33*,
1245 3645–3647.

1246 150. Morahan, G., Balmer, L., and Monley, D. (2008). Establishment of "The Gene Mine": a resource for

1247 rapid identification of complex trait genes. Mamm. Genome *19*, 390–393.

1248 151. Jansen, B.C., Falck, D., de Haan, N., Hipgrave Ederveen, A.L., Razdorov, G., Lauc, G., and Wuhrer, M.
1249 (2016). LaCyTools: A Targeted Liquid Chromatography–Mass Spectrometry Data Processing Package
1250 for Relative Quantitation of Glycopeptides. J. Proteome Res. *15*, 2198–2210.

1251 152. He, L., Diedrich, J., Chu, Y.-Y., and Yates, J.R., 3rd (2015). Extracting accurate precursor information
1252 for tandem mass spectra by RawConverter. Anal. Chem. *87*, 11361–11367.

1253 153. Xu, T., Park, S.K., Venable, J.D., Wohlschlegel, J.A., Diedrich, J.K., Cociorva, D., Lu, B., Liao, L., Hewel,
1254 J., Han, X., et al. (2015). ProLuCID: An improved SEQUEST-like algorithm with enhanced sensitivity
1255 and specificity. J. Proteomics *129*, 16–24.

1256 154. Tabb, D.L., McDonald, W.H., and Yates, J.R., 3rd (2002). DTASelect and Contrast: tools for
1257 assembling and comparing protein identifications from shotgun proteomics. J. Proteome Res. *1*,
1258 21–26.

1259 155. Peng, J., Elias, J.E., Thoreen, C.C., Licklider, L.J., and Gygi, S.P. (2003). Evaluation of
1260 multidimensional chromatography coupled with tandem mass spectrometry (LC/LC-MS/MS) for
1261 large-scale protein analysis: the yeast proteome. J. Proteome Res. *2*, 43–50.

1262 156. Park, S.K., Venable, J.D., Xu, T., and Yates, J.R., 3rd (2008). A quantitative analysis software tool for
1263 mass spectrometry-based proteomics. Nat. Methods *5*, 319–322.

1264 157. Irvine, E.B., Peters, J.M., Lu, R., Grace, P.S., Sixsmith, J., Wallace, A., Schneider, M., Shin, S.,
1265 Karpinski, W., Hsiao, J.C., et al. (2022). Fc-engineered antibodies leverage neutrophils to drive
1266 control of *Mycobacterium tuberculosis*. bioRxiv. 10.1101/2022.05.01.490220.

1267 158. Engler, C., and Marillonnet, S. (2014). Golden Gate cloning. Methods Mol. Biol. *1116*, 119–131.

1268 159. Fang, J., Qian, J.-J., Yi, S., Harding, T.C., Tu, G.H., VanRoey, M., and Jooss, K. (2005). Stable antibody
1269 expression at therapeutic levels using the 2A peptide. Nat. Biotechnol. *23*, 584–590.

1270 160. Mahan, A.E., Tedesco, J., Dionne, K., Baruah, K., Cheng, H.D., De Jager, P.L., Barouch, D.H.,
1271 Suscovich, T., Ackerman, M., Crispin, M., et al. (2015). A method for high-throughput, sensitive
1272 analysis of IgG Fc and Fab glycosylation by capillary electrophoresis. J. Immunol. Methods *417*, 34–
1273 44.

1274 161. Benjamini, Y., and Hochberg, Y. (1995). Controlling the False Discovery Rate: A Practical and
1275 Powerful Approach to Multiple Testing. J. R. Stat. Soc. Series B Stat. Methodol. *57*, 289–300.

1276 162. Xu, C., and Ng, D.T.W. (2015). Glycosylation-directed quality control of protein folding. Nat. Rev.
1277 Mol. Cell Biol. *16*, 742–752.

1278 163. Shental-Bechor, D., and Levy, Y. (2008). Effect of glycosylation on protein folding: a close look at
1279 thermodynamic stabilization. Proc. Natl. Acad. Sci. U. S. A. *105*, 8256–8261.

1280 164. Shihab, H.A., Gough, J., Mort, M., Cooper, D.N., Day, I.N.M., and Gaunt, T.R. (2014). Ranking non-
1281 synonymous single nucleotide polymorphisms based on disease concepts. Hum. Genomics *8*, 11.

1282 165. Shihab, H.A., Gough, J., Cooper, D.N., Day, I.N.M., and Gaunt, T.R. (2013). Predicting the functional
1283 consequences of cancer-associated amino acid substitutions. Bioinformatics *29*, 1504–1510.

1284 166. Shihab, H.A., Gough, J., Cooper, D.N., Stenson, P.D., Barker, G.L.A., Edwards, K.J., Day, I.N.M., and
1285 Gaunt, T.R. (2013). Predicting the functional, molecular, and phenotypic consequences of amino
1286 acid substitutions using hidden Markov models. Hum. Mutat. *34*, 57–65.

1287 167. Baković, M.P., Selman, M.H.J., Hoffmann, M., Rudan, I., Campbell, H., Deelder, A.M., Lauc, G., and
1288 Wuhrer, M. (2013). High-throughput IgG Fc N-glycosylation profiling by mass spectrometry of
1289 glycopeptides. J. Proteome Res. *12*, 821–831.

1290 168. Pucić, M., Knezević, A., Vidic, J., Adamczyk, B., Novokmet, M., Polasek, O., Gornik, O., Supraha-
1291 Goreta, S., Wormald, M.R., Redzić, I., et al. (2011). High throughput isolation and glycosylation
1292 analysis of IgG-variability and heritability of the IgG glycome in three isolated human populations.
1293 Mol. Cell. Proteomics *10*, M111.010090.

1294 169. Klarić, L., Tsepilov, Y.A., Stanton, C.M., Mangino, M., Sikka, T.T., Esko, T., Pakhomov, E., Salo, P.,
1295 Deelen, J., McGurnaghan, S.J., et al. (2020). Glycosylation of immunoglobulin G is regulated by a
1296 large network of genes pleiotropic with inflammatory diseases. Sci. Adv. *6*, eaax0301.

1297 170. Rose, R.J., van Berkel, P.H.C., van den Bremer, E.T.J., Labrijn, A.F., Vink, T., Schuurman, J., Heck,
1298 A.J.R., and Parren, P.W.H.I. (2013). Mutation of Y407 in the CH3 domain dramatically alters
1299 glycosylation and structure of human IgG. MAbs *5*, 219–228.

1300 171. Vidarsson, G., Dekkers, G., and Rispens, T. (2014). IgG subclasses and allotypes: from structure to
1301 effector functions. Front. Immunol. *5*, 520.

1302 172. Hutton, S.M., and Spritz, R.A. (2008). Comprehensive analysis of oculocutaneous albinism among
1303 non-Hispanic caucasians shows that OCA1 is the most prevalent OCA type. J. Invest. Dermatol. *128*,
1304 2442–2450.

1305 173. Rademacher, C., Bru, T., McBride, R., Robison, E., Nycholat, C.M., Kremer, E.J., and Paulson, J.C.
1306 (2012). A Siglec-like sialic-acid-binding motif revealed in an adenovirus capsid protein. Glycobiology
1307 *22*, 1086–1091.

1308 174. Chavent, M., Kuentz-Simonet, V., Labenne, A., and Saracco, J. (2014). Multivariate analysis of mixed
1309 data: The R package PCAmixdata. arXiv [stat.CO].

Standard Templating

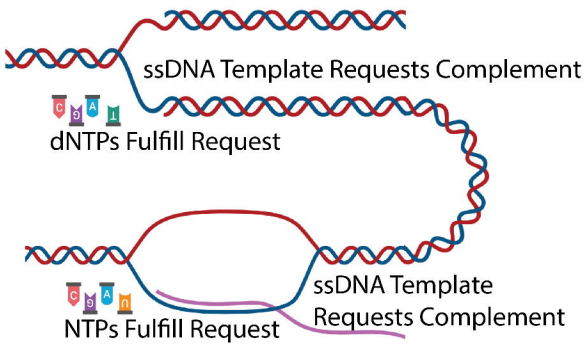

Glycoprotein Structure Requests

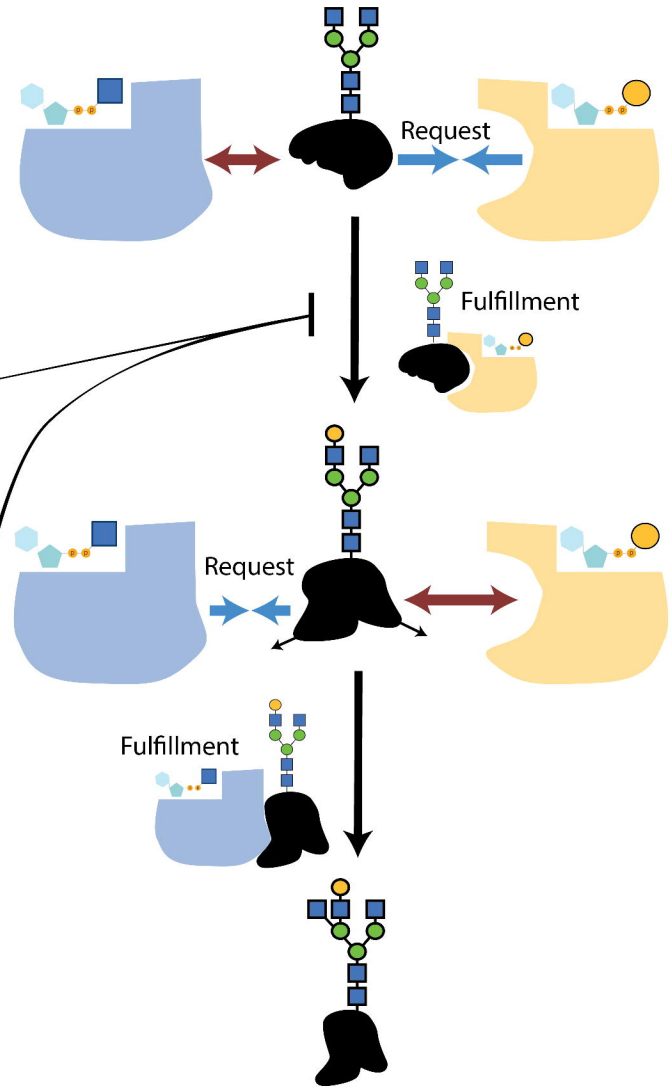

Validation Types

Computational

Retrospective Experiments

Novel Experiments

Specific Applications

Pathogenic Variants

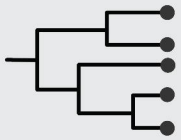

Evolutionary Statistics

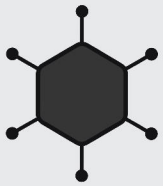

Viral Proteins

Antibodies

Precursor-limited Fulfillment

Glycan Acceptor Availibility;
Upstream failure

Charged Nucleotide Sugar Availability
Monosaccharide Transporter Expression

Glycosyltransferase Expression

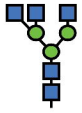

Competitive Inhibition
Common Acceptors

Classical Non-Templated Glycosylation

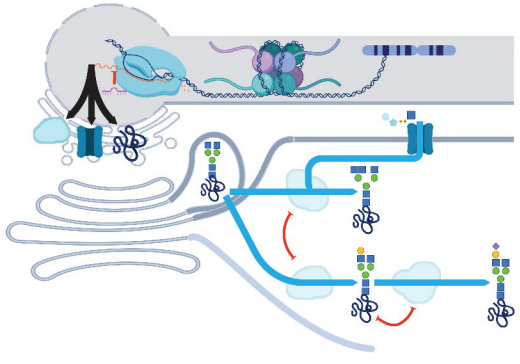

Environmental constraints:
Expression, precursor, competition

Additional Glycosylation Constraints: Protein Structure

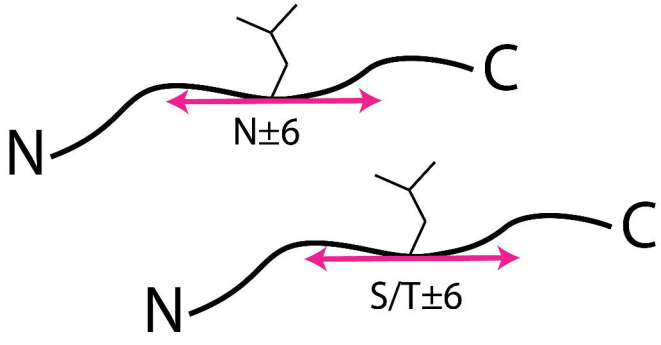

2D structure: amino acids and chemistry sequentially close to N- and O-Glycosites

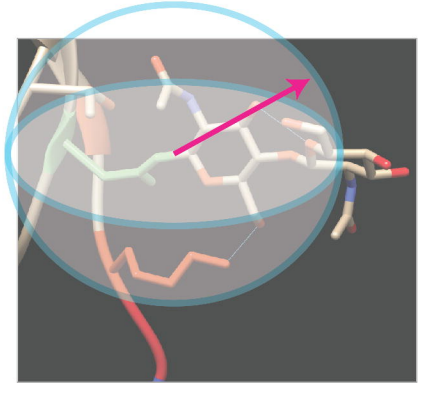

3D structure: amino acids, secondary structure, accessibility, depth, and chemistry spatially close to N- and O-Glycosites

Protein structure features close (2D and 3D) to N- and O-Glycosites (modeled seperately) constrain glycosylation

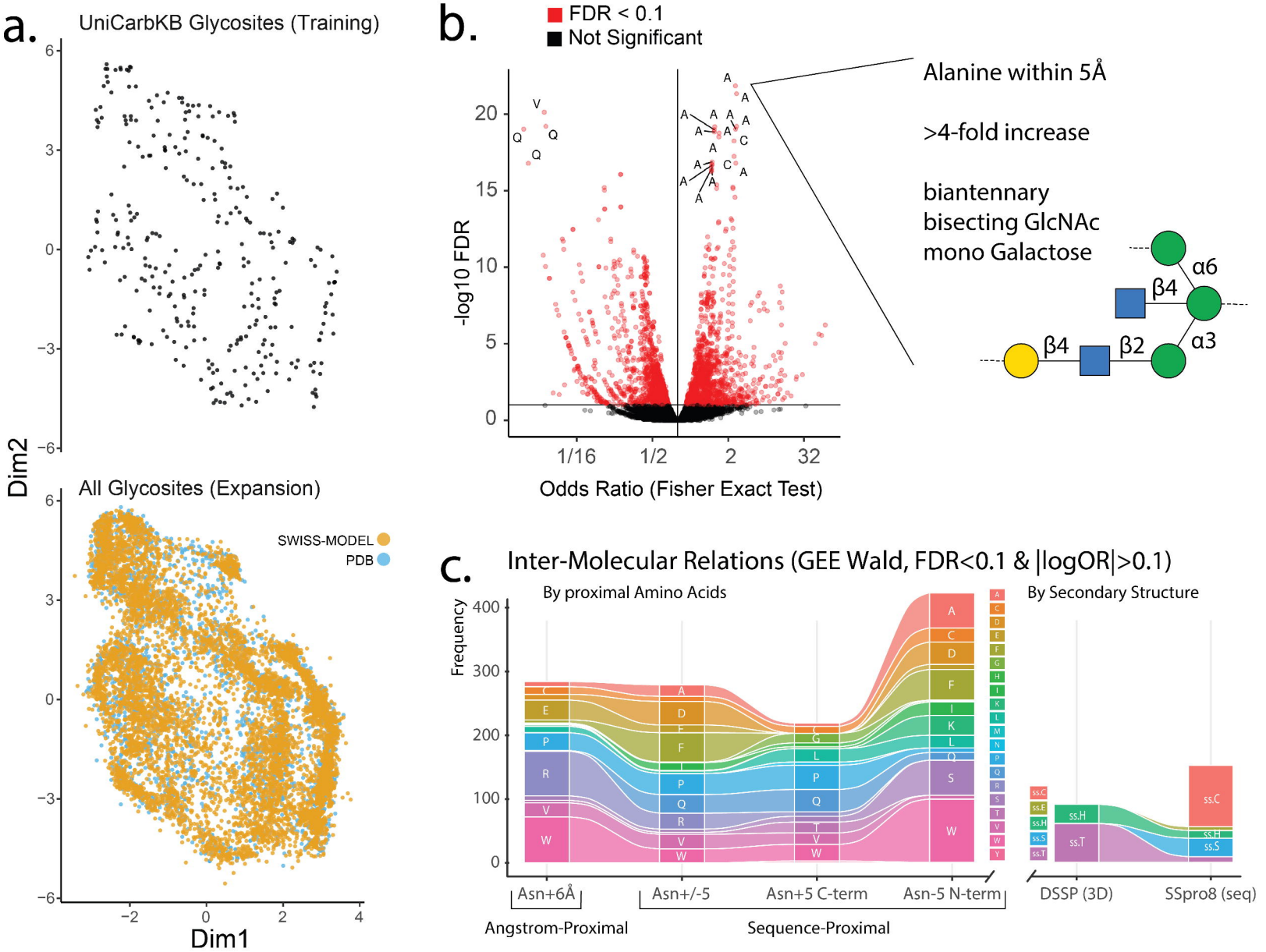
a.
UniCarbKB Glycosites (Training)
All Glycosites (Expansion)
SWISS-MODEL
PDB
Dim1
Dim2
b.
FDR < 0.1
Not Significant
-log10 FDR
Odds Ratio (Fisher Exact Test)
1/16
1/2
2
32
Alanine within 5Å
>4-fold increase
biantennary
bisecting GlcNAc
mono Galactose
α6
β4
β4
β2
α3
c.
Inter-Molecular Relations (GEE Wald, FDR<0.1 & |logOR|>0.1)
By proximal Amino Acids
By Secondary Structure
Frequency
Asn+6Å
Asn+/-5
Asn+5 C-term
Asn-5 N-term
DSSP (3D)
SSpro8 (seq)
Angstrom-Proximal
Sequence-Proximal

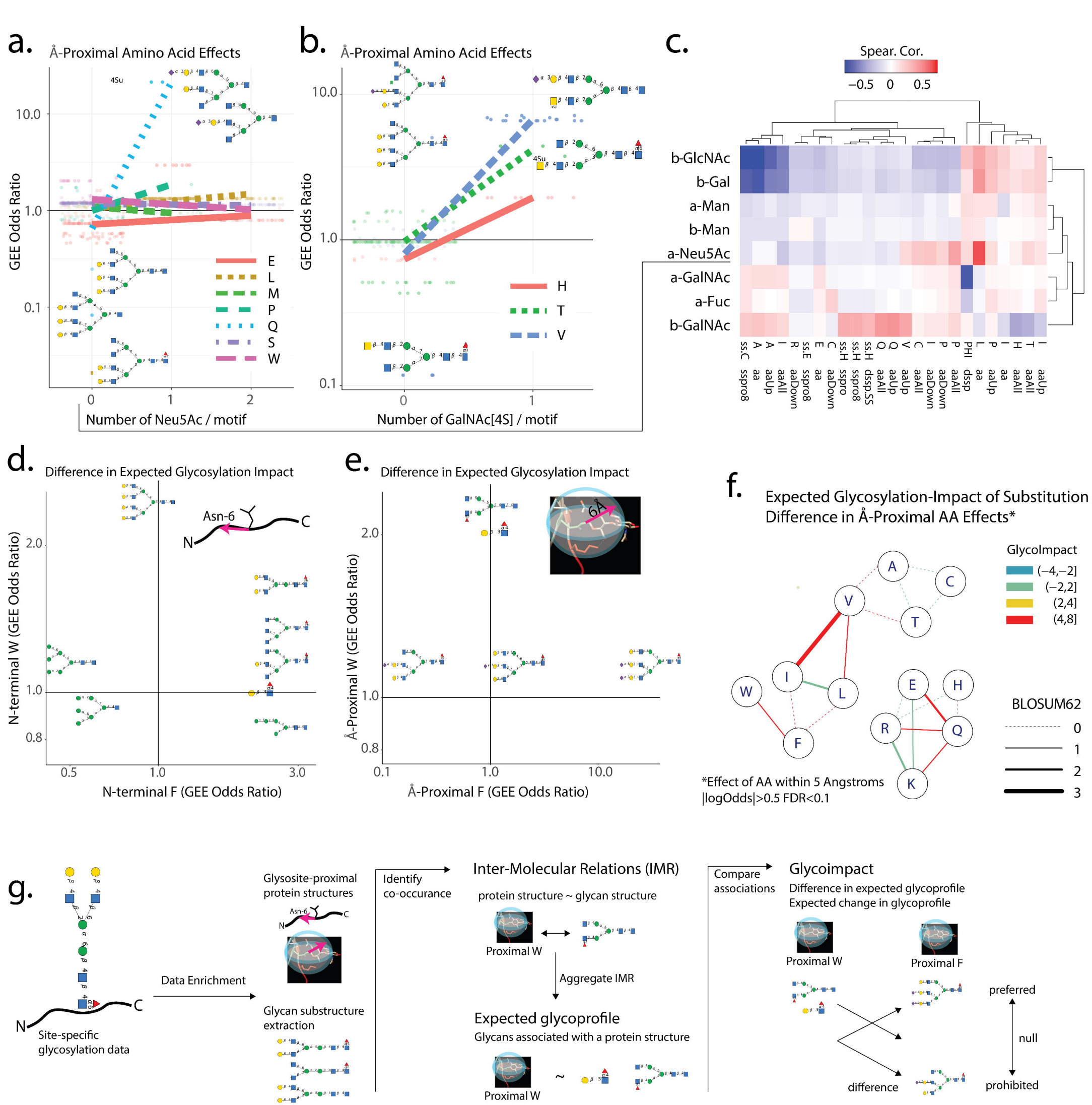
a.
Å-Proximal Amino Acid Effects
GEE Odds Ratio
Number of Neu5Ac / motif
E
L
M
P
Q
S
W
b.
Å-Proximal Amino Acid Effects
GEE Odds Ratio
Number of GalNAc[4S] / motif
H
T
V
c.
Spear. Cor.
−0.5 0 0.5
b-GlcNAc
b-Gal
a-Man
b-Man
a-Neu5Ac
a-GalNAc
a-Fuc
b-GalNAc
d.
Difference in Expected Glycosylation Impact
N-terminal W (GEE Odds Ratio)
N-terminal F (GEE Odds Ratio)
Asn-6
N
C
e.
Difference in Expected Glycosylation Impact
Å-Proximal W (GEE Odds Ratio)
Å-Proximal F (GEE Odds Ratio)
6Å
f.
Expected Glycosylation-Impact of Substitution
Difference in Å-Proximal AA Effects*
GlycoImpact
(−4,−2]
(−2,2]
(2,4]
(4,8]
BLOSUM62
0
1
2
3
*Effect of AA within 5 Angstroms
|logOdds|>0.5 FDR<0.1
g.
Site-specific glycosylation data
Data Enrichment
Glysosite-proximal protein structures
Glycan substructure extraction
Identify co-occurance
Inter-Molecular Relations (IMR)
protein structure ~ glycan structure
Proximal W
Aggregate IMR
Expected glycoprofile
Glycans associated with a protein structure
Compare associations
Glycoimpact
Difference in expected glycoprofile
Expected change in glycoprofile
Proximal F
preferred
null
prohibited
difference

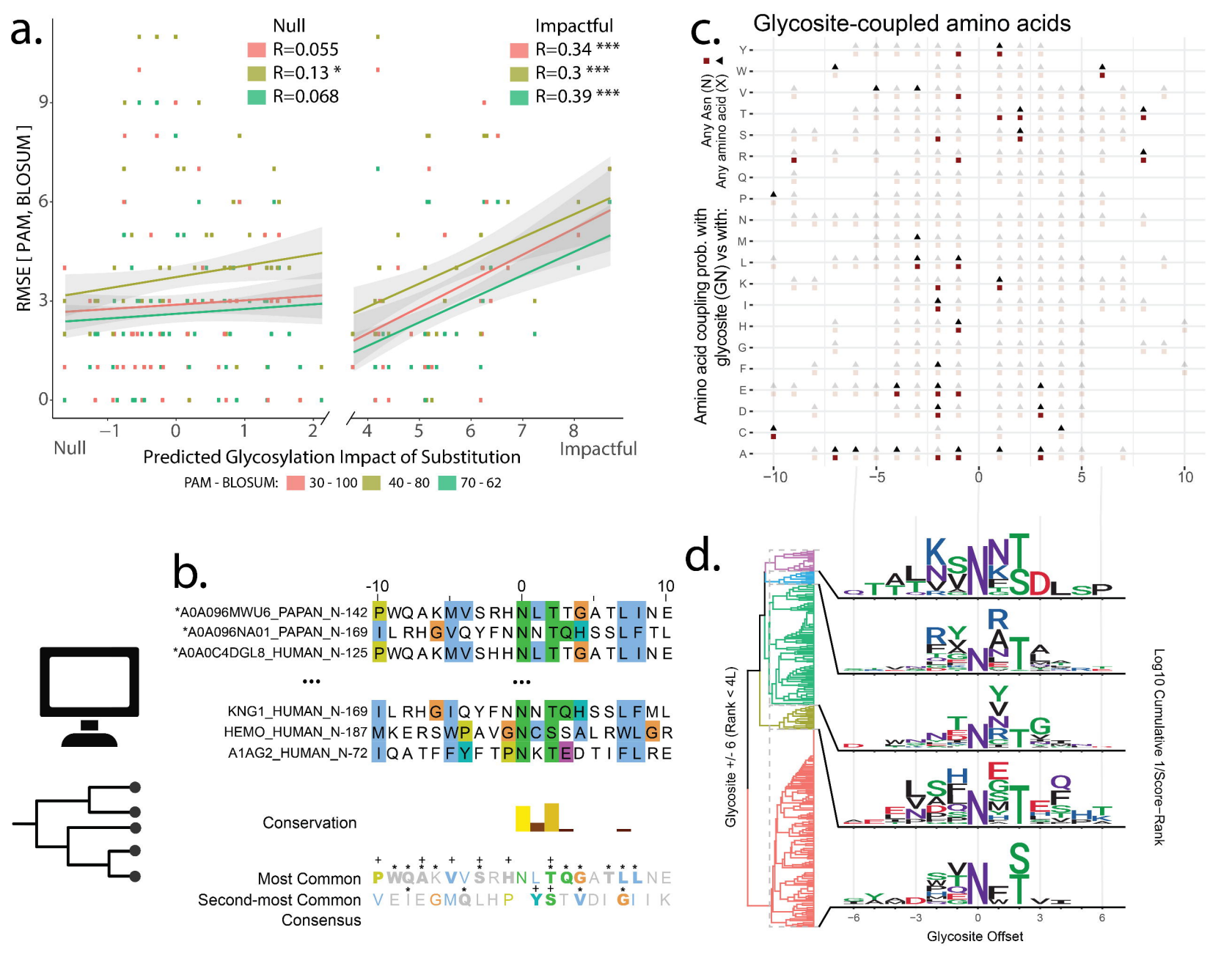
a.
Null
R=0.055
R=0.13 *
R=0.068
Impactful
R=0.34 ***
R=0.3 ***
R=0.39 ***
RMSE [PAM, BLOSUM]
Null
Impactful
Predicted Glycosylation Impact of Substitution
PAM - BLOSUM: 30 - 100 40 - 80 70 - 62
c.
Glycosite-coupled amino acids
Any Asn (N)
Any amino acid (X)
Amino acid coupling prob. with glycosite (GN) vs with:
b.
*A0A096MWU6_PAPAN_N-142
*A0A096NA01_PAPAN_N-169
*A0A0C4DGL8_HUMAN_N-125
KNG1_HUMAN_N-169
HEMO_HUMAN_N-187
A1AG2_HUMAN_N-72
Conservation
Most Common
Second-most Common
Consensus
d.
Glycosite +/- 6 (Rank < 4L)
Log10 Cumulative 1/Score−Rank
Glycosite Offset

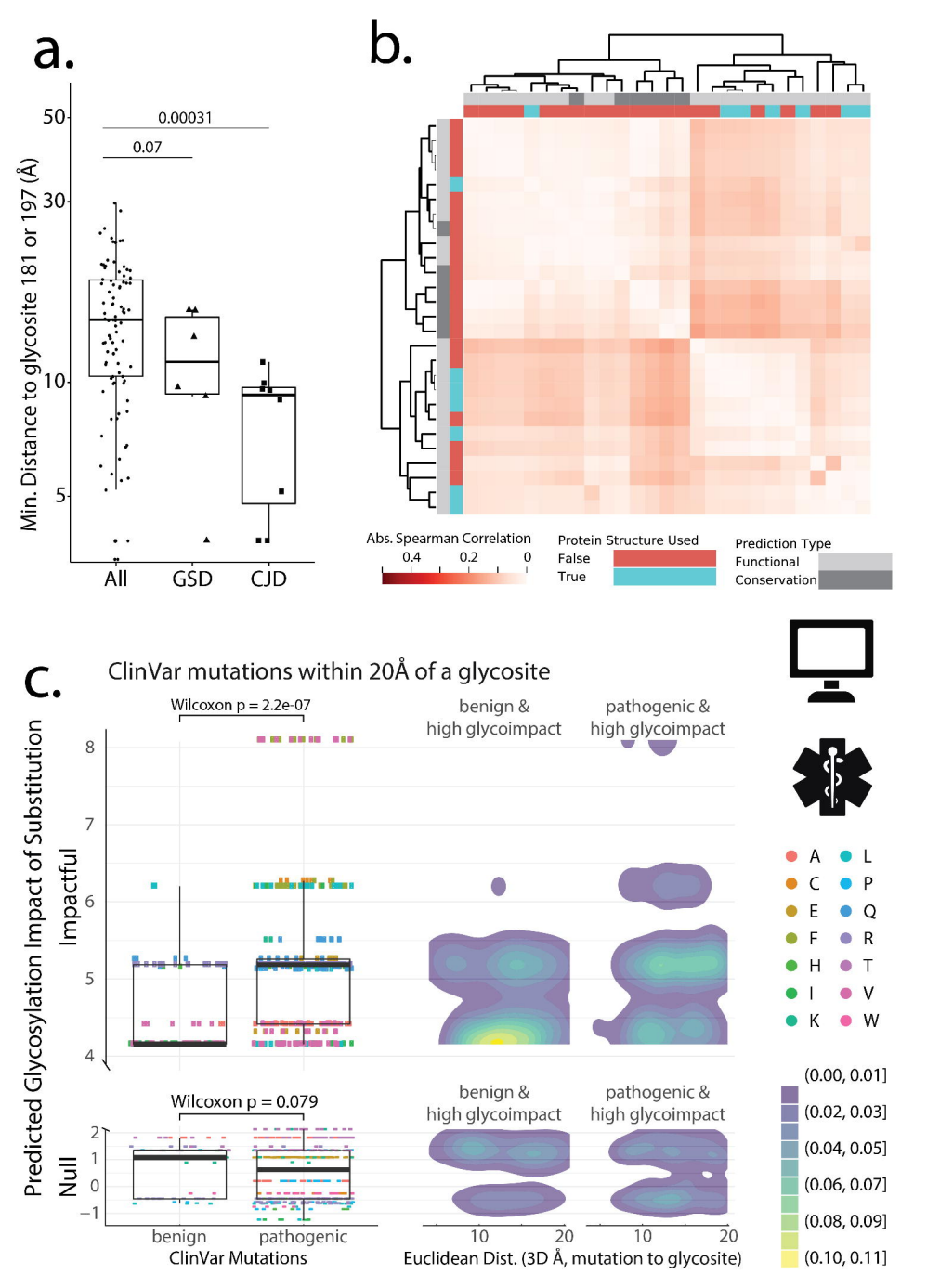
a.
0.00031
0.07
Min. Distance to glycosite 181 or 197 (Å)
50
30
10
5
All
GSD
CJD
b.
Abs. Spearman Correlation
0.4
0.2
0
Protein Structure Used
False
True
Prediction Type
Functional
Conservation
c.
ClinVar mutations within 20Å of a glycosite
Wilcoxon p = 2.2e-07
benign &
high glycoimpact
pathogenic &
high glycoimpact
Predicted Glycosylation Impact of Substitution
Impactful
Null
Wilcoxon p = 0.079
benign
pathogenic
ClinVar Mutations
Euclidean Dist. (3D Å, mutation to glycosite)
A
C
E
F
H
I
K
L
P
Q
R
T
V
W
(0.00, 0.01]
(0.02, 0.03]
(0.04, 0.05]
(0.06, 0.07]
(0.08, 0.09]
(0.10, 0.11]

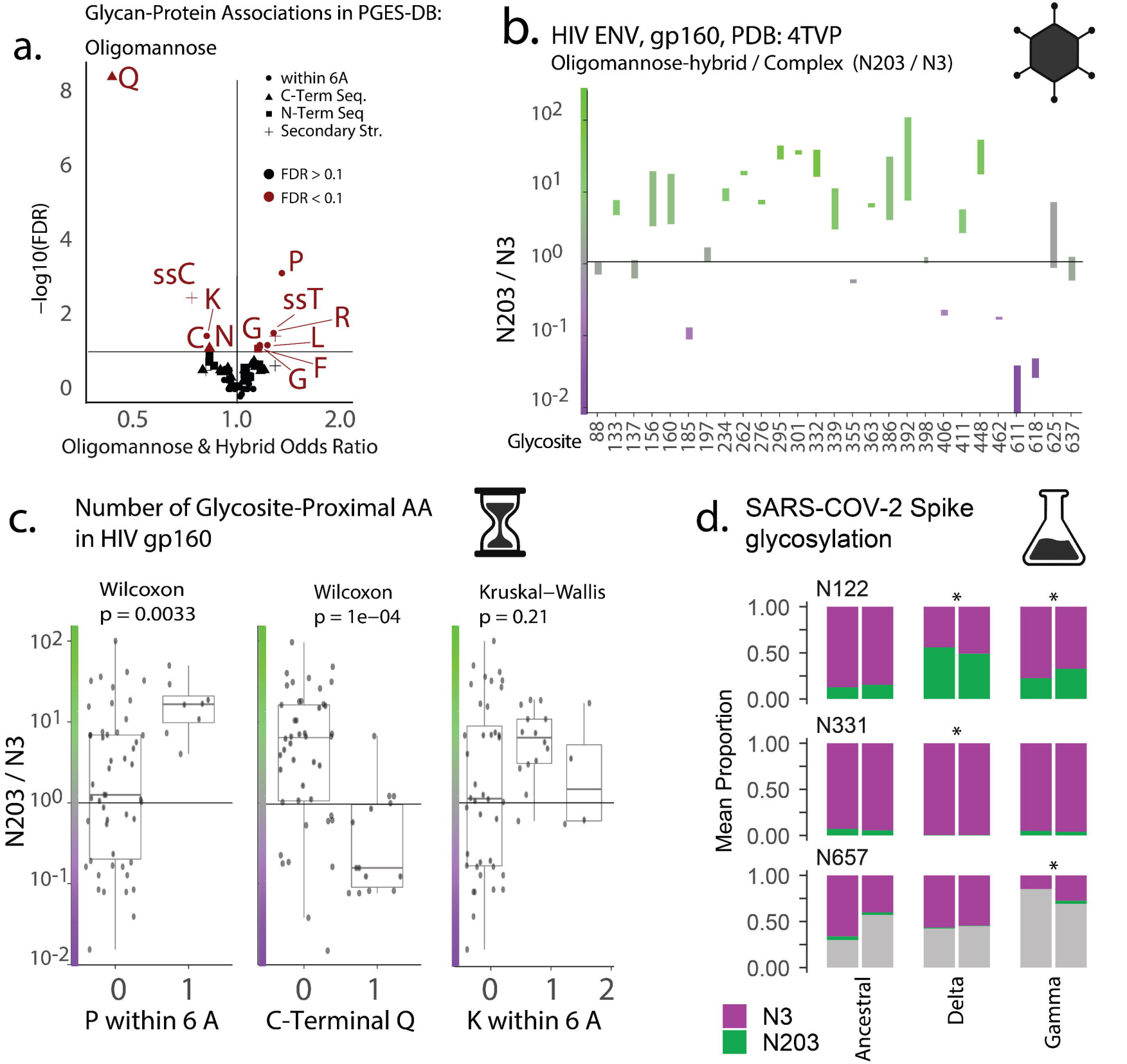
a.
Glycan-Protein Associations in PGES-DB:
Oligomannose
within 6A
C-Term Seq.
N-Term Seq
Secondary Str.
FDR > 0.1
FDR < 0.1
Q
ssC
K
C
N
G
P
ssT
R
L
F
G
−log10(FDR)
Oligomannose & Hybrid Odds Ratio
b.
HIV ENV, gp160, PDB: 4TVP
Oligomannose-hybrid / Complex (N203 / N3)
N203 / N3
Glycosite
88 133 137 156 160 185 197 234 262 276 295 301 332 339 355 363 386 392 398 406 411 448 462 611 618 625 637
c.
Number of Glycosite-Proximal AA in HIV gp160
Wilcoxon p = 0.0033
Wilcoxon p = 1e−04
Kruskal−Wallis p = 0.21
N203 / N3
P within 6 A
C-Terminal Q
K within 6 A
d.
SARS-COV-2 Spike glycosylation
N122
N331
N657
Mean Proportion
N3
N203
Ancestral
Delta
Gamma

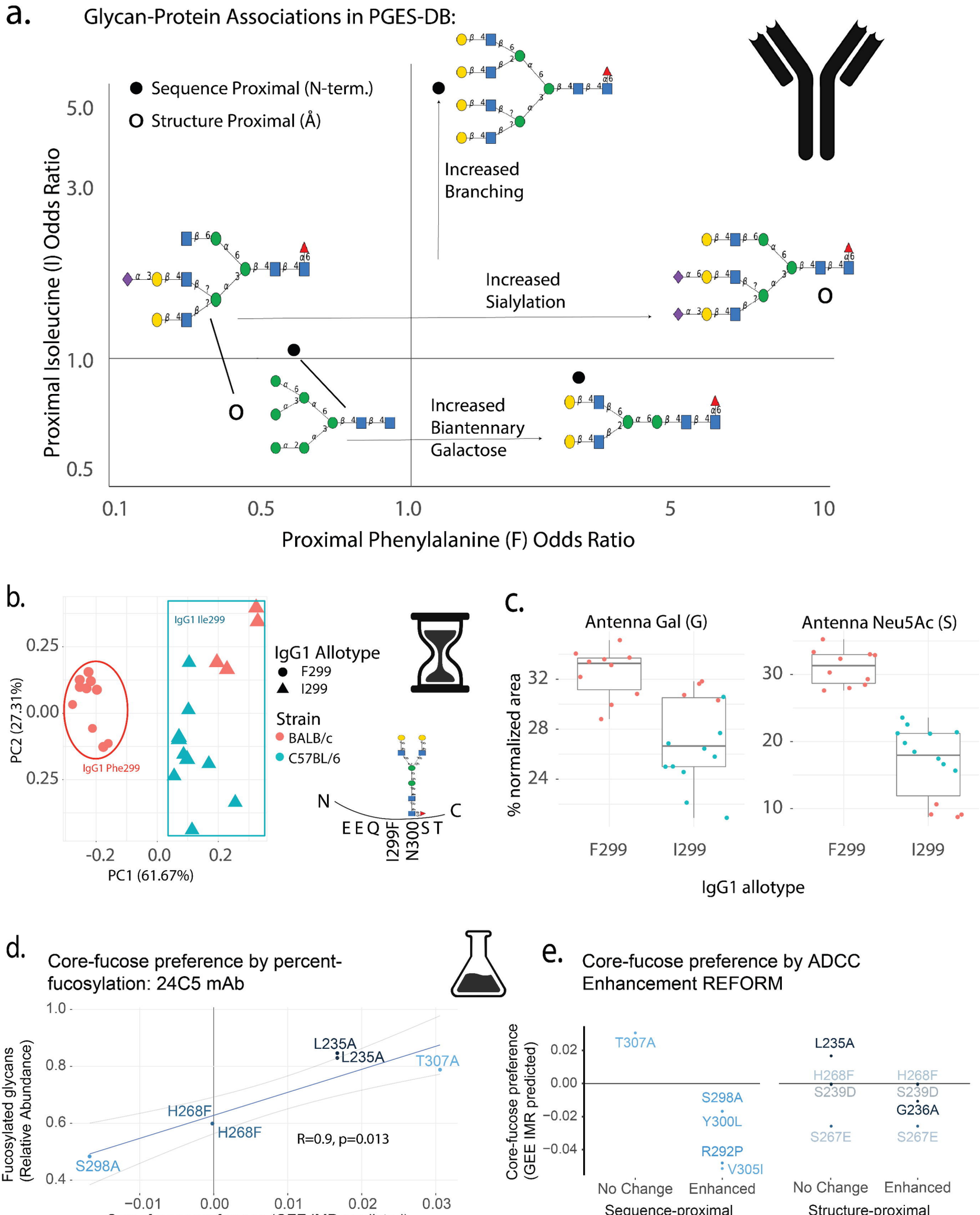
a.
Glycan-Protein Associations in PGES-DB:
Sequence Proximal (N-term.)
Structure Proximal (Å)
Increased Branching
Increased Sialylation
Increased Biantennary Galactose
Proximal Isoleucine (I) Odds Ratio
Proximal Phenylalanine (F) Odds Ratio
5.0
3.0
1.0
0.5
0.1
0.5
1.0
5
10
b.
IgG1 Ile299
IgG1 Phe299
PC2 (27.31%)
PC1 (61.67%)
0.25
0.00
0.25
-0.2
0.0
0.2
IgG1 Allotype
F299
I299
Strain
BALB/c
C57BL/6
N
C
EEQ
I299F
N300
ST
c.
Antenna Gal (G)
Antenna Neu5Ac (S)
% normalized area
32
28
24
30
20
10
F299
I299
IgG1 allotype
d.
Core-fucose preference by percent-fucosylation: 24C5 mAb
Fucosylated glycans (Relative Abundance)
1.0
0.8
0.6
0.4
L235A
L235A
T307A
H268F
H268F
S298A
R=0.9, p=0.013
−0.01
0.00
0.01
0.02
0.03
Core−fucose preference (GEE IMR predicted)
e.
Core-fucose preference by ADCC Enhancement REFORM
Core-fucose preference (GEE IMR predicted)
0.02
0.00
−0.02
−0.04
T307A
S298A
Y300L
R292P
V305I
L235A
H268F
S239D
S267E
H268F
S239D
G236A
S267E
No Change
Enhanced
Sequence-proximal
No Change
Enhanced
Structure-proximal